NTNU – Trondheim
Norwegian University of
Science and Technology

Development and Verification of a Gesilinger Flexible Coupling Bond Graph Model

Bjørn Eliassen Vik

Marine Technology (2-year)
Submission date: June 2014
Supervisor: Eilif Pedersen, IMT

Norwegian University of Science and Technology
Department of Marine Technology

NTNU Trondheim
Norwegian University of Science and Technology
Department of Marine Technology

MASTER THESIS, SPRING 2014

for

Stud.tech. Bjørn Eliassen Vik

Development and Verification of a Gesilinger Flexible Coupling Bond Graph Model

(Utvikling og verifisering av en Geislinger fleksibel kobling båndgrafmodell)

There has been an increase in ship traffic in Arctic waters the later years, this challenges today's ship design. One of the challenges is the contact loads that occur, due to ice blocks encountering the ship propeller. The ice propeller interaction is a complicated process, and more knowledge on the effect of the ice propeller interaction on the ship propulsion drive train is needed.

This master thesis focus on improving the dynamic mathematical model of one of the ship propulsion drive train components, namely the flexible coupling.

The scope of this master thesis includes:

- Develop a mathematical model of the Geislinger flexible coupling using the bond graph approach. The model should include the effects of the radially aligned spring and the oil transfer between the oil chambers. The model is to be implemented in to the 20-sim simulation software.
- Compare the model to the empirically found dynamic stiffness and damping provided by the coupling manufacturer.
- Investigate the effect of changing the model parameters on the dynamic stiffness and damping.
- Implement the mathematical model of the Geislinger coupling in to a marine propulsion drive train, where the propeller is to be subjected by representative ice propeller interaction loads.
- Compare the drive train model including the mathematical model of the Geislinger flexible coupling to existing model.

Additional analyses might also show to be of interest during the work

The work may show to be more extensive than anticipated. Some topics may therefore be left out after discussion with the supervisor without any negative influence on the grading.

The candidate should in her/his report give a personal contribution to the solution of the problem formulated in this text. All assumptions and conclusions must be supported by mathematical

models and/or references to physical effects in a logical manner. The candidate should apply all available sources to find relevant literature and information on the actual problem.

The report should be well organised and give a clear presentation of the work and all conclusions. It is important that the text is well written and that tables and figures are used to support the verbal presentation. The report should be complete, but still as short as possible.

The final report must contain this text, an acknowledgement, summary, main body, conclusions and suggestions for further work, symbol list, references and appendices. All figures, tables and equations must be identified by numbers. References should be given by author name and year in the text, and presented alphabetically by name in the reference list. The re-port must be submitted in two copies unless otherwise has been agreed with the supervisor.

From the report it should be possible to identify the work carried out by the candidate and what has been found in the available literature. It is important to give references to the original source for theories and experimental results. The report should be delivered according to instructions from the faculty, and - if needed – additional material (binder, VD/CD/memory stick) should be delivered to the supervisor.

The work will be carried out in cooperation with a Ph.D.-project at NTNU

Ph.D. candidate Drazen Polic

Deadline: 10 June 2014

Eilif Pedersen
Supervisor

Abstract

There has been an increase in ship traffic in Arctic waters the later years, this challenges today's ship design. One of the challenges is the contact loads that occur, due to ice blocks encountering the ship propeller. The ice propeller interaction is a complicated process, and more knowledge on the effect of the ice propeller interaction on the ship propulsion drive train is needed.

This master thesis focus on improving the dynamic mathematical model of one of the ship propulsion drive train components, namely the flexible coupling. The model developed is based on the Geislinger flexible coupling, and is developed using the bond graph approach with the 20-sim simulation software. It takes in to account the major dynamic effects of the radially aligned springs and the oil flow between the oil chambers.

Simulations show that the dynamic stiffness and damping coefficient of the flexible coupling model developed in this project, is heavily dependent on the deflection frequency and velocity. Both the damping factor and stiffness increases with frequency. This is due to an increase in both the amount of oil that is compressed, and the pressure difference between the oil chambers increases, with increasing deflection velocity.

Simulations show that the static stiffness is mainly dependent on the geometry of the radially aligned springs, and that the dynamic stiffness is heavily dependent on the coefficient of discharge describing the oil flow between the oil chambers of the coupling.

The coupling model was implemented in to a marine propulsion drive train established in another project, which was subjected to torsional ice impact loads, and compared to the original model. Simulations did show that the oil compressibility caused the flexible coupling to become stiffer than the reference model, during the rapid change of oil chamber volume. While the oil chamber volume change was less, the flexible coupling became less stiff than the reference model.

It is recommended that the tapering of the radially aligned springs is included in the model as this affects the flexible coupling stiffness, especially during impact loads. Also it is recommended that CFD simulations are performed to verify the coefficient of discharge used in the model.

Sammendrag

Den økte skipstrafikken de senere år stiller økte krav til dagens skipsdesign. En av utfordringene er kontaktkreftene som oppstår i det isblokker treffer propellen til skipet. Propell-is-interaksjonen er en komplisert prosess og det trengs mer kunnskap angående effekten propell-is-interaksjonen har på skipets framdriftsmaskinerisystem. Denne masteroppgaven fokuserer på å forbedre den matematiske modellen som beskriver en av komponentene i framdriftsmaskinerisystemet, nemlig den elastiske koblingen mellom propellakslingen og framdriftsmaskinen.

Den matematiske modellen som beskriver dynamikken til den elastiske koblingen er utviklet basert på den elastiske koblingen produsert av Geislinger, og er utviklet ved å bruke båndgrafmetoden i simuleringsprogrammet 20-sim. Hovedeffektene som inngår i modellen er den statiske og dynamiske stivheten til de radielle fjærene som inngår i den elastiske koblingen, og effekten fra oljen som befinner seg i kamrene rundt fjærene.

Simuleringer viser at den dynamiske stivheten og dempningsfaktoren til den elastiske koblingen, avhenger av hastigheten og frekvensen som koblingen vrides med. Både dynamisk stivhet og dempingsfaktor øker med frekvens. Dette kommer av at mengden av olje som komprimeres og trykkforskjellen mellom oljekamrene øker ved økende vridningsfrekvens og hastighet.

I tillegg viser simuleringer at den statiske stivheten er hovedsakelig avhengig av geometrien til radialfjærene, og at den dynamiske stivheten er i stor grad avhengig av oljegjennomstrømningskoeffisienten som beskriver størrelsen på oljestrømmen pga. trykforskjell mellom oljekamrene.

Båndgrafmodellen av den elastiske koblingen ble implementert i en båndgrafmodell av et framdriftsmaskinerisystem etablert i et annet prosjekt. Framdriftsmaskinerisystemet ble utsatt for lastene som oppstår ved is-propell-interaksjoner og sammenlignet med den originale modellen. Simuleringer viser at på grunn av oljens kompressibilitet blir stivheten til den elastiske koblingen større når volumendringen av kammeret er stor, og mindre når volumendringen er liten, i forhold til sammenligningsmodellen.

Det anbefales å inkludere radial fjærer med varierende tverrsnittsareal ettersom dette vil være spesielt viktig ved impulslaster. I tillegg anbefales det å foreta CFD simuleringer for å verifisere oljegjennomstrømingskoeffisienten.

Contents

List of Figures

List of Tables

Chapter 1
Introduction

1.1 Background

There has been an increase in ship traffic in Arctic waters the later years. One reason for this, is that the northern sea route was opened by the Russian federation for traffic in 2009 (Erikstad and Ehlers, 2012). Another reason is the development of oil fields in the Barents Sea.

Ships operating in Arctic waters will encounter ice and the challenges caused by ice ship interactions. Examples of such challenges are the increased resistance which leads to increasing propulsion demands, increased loads acting on the ship hull which leads to higher strength demands.

Another challenge is when ice blocks come in contact with the ship propeller. This happens as ice blocks collide with the ship bow and get submerged. As the ship advance in the water, the ice pieces are brought in to the vicinity of the propeller and are sucked into the propeller. The propeller hits the ice block and the ice block is crushed. An illustration of this is shown in figure 1.1. The ice propeller interaction may cause bending and breakage of the propeller due to the impact. In addition, the ice propeller interaction is a cyclic load, which with the right frequency and magnitude may lead to noise or harmful vibrations in the propulsion drive train. The harmful vibrations may occur if loads from the propeller ice interaction has harmonic components, close to a natural frequency, of the propulsion drive train.

The propulsion drive train referred to here is a marine propulsion drive train consisting of a engine, propeller shaft, flexible coupling and a propeller.

To ensure safe and reliable operations, the harmful vibrations must be avoided. This is done by careful design of the propulsion drive train using proper modelling tools, which account for the most important dynamics of the propulsion drive train

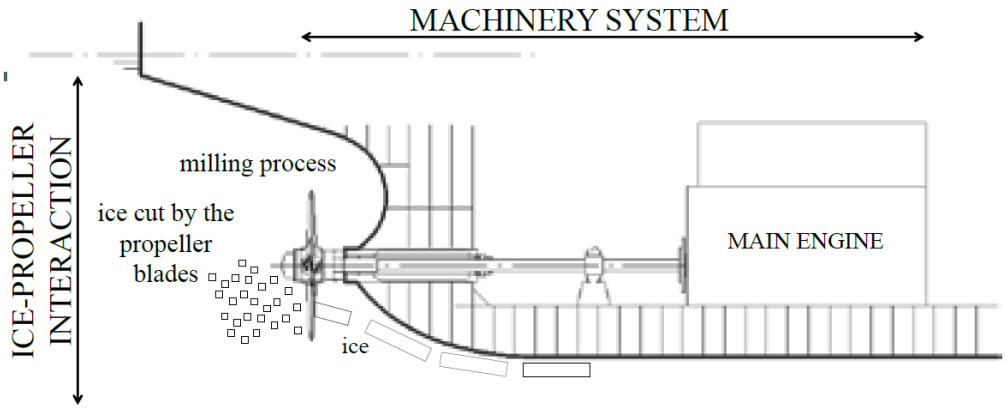

Figure 1.1: Figure showing a marine propulsion drive train being subjected to ice impact loads (Polic et al., 2013)

The ice-induced vibrations is most likely to be harmful when the propulsion drive train operates at frequencies close to resonance. At these operating conditions, the system response is mainly controlled by damping. The vibration damper is one of the major components of the propulsion drive train exerting damping behaviour. For this reason, the damper is one of the main components controlling the propulsion drive trains response when operating in frequencies close to resonance.

1.2 Scope

The scope of this master thesis includes:

- Develop a mathematical model of the Geislinger flexible coupling using the bond graph approach. The model should include the effects of the radially aligned spring and the oil transfer between the oil chambers. The model is to be implemented in to the 20-sim simulation software.
- Compare the model to the empirically found dynamic stiffness and damping provided by the coupling manufacturer.
- Investigate the effect of changing the model parameters on the dynamic stiffness and damping.
- Implement the mathematical model of the Geislinger coupling in to a marine propulsion drive train, where the propeller is to be subjected by representative ice propeller interaction loads.

- Compare the drive train model including the mathematical model of the Geislinger flexible coupling to existing model.

1.3 Thesis structure

- In chapter 1 the context of the problem is established and the problem to be solved is explain.
- In chapter 2 the theory which is needed for developing the flexible coupling and the drive train model is explained.
- In chapter 3 the development of the flexible coupling model is explained.
- In chapter 4 the model parameters is established and the model behaviour is verified.
- In chapter 5 the Geislinger flexible coupling bond graph model is implemented in a marine propulsion drive train bond graph model and a simulation case is performed.
- In chapter 6 are conclusions and recommendations for further work presented.

Chapter 2

Theory

2.1 Classification Requirements

One of the reasons for the need of a proper model of the flexible coupling is the requirements of classification societies.

To operate in Arctic water, ships will have to comply with certain classification requirements and rules. One of the classification societies that offers to classify ships for this purpose is DNV GL.

In the rules for classification of ships part 5 chapter 1 (DNV, 2013b), the classification impose requirements regarding the propulsion drive train. One of the requirements is that the maximum response torque along the propeller shaft line Q_r shall be determined through a detailed vibration analysis. This is if there exist harmful resonances at a first order blade frequency within the operating range of the propulsion drive train with a 20% margin.

The maximum response torque serves as a design requirement for all the major components of the propulsion drive train: intermediate shaft, flexible coupling, reduction gears, crank shafts, flange connections, shrink fit connections etc.

DNV GL requires that the ice induced torsional loads are described as a series of blade impacts which is half sine shaped pulses. A more thorough discussion of the ice induced torque is done in section 2.4

Both to ensure that harmful resonances doesn't occur and to find the maximum response torque, accurate models of the major components of the propulsion drive train is needed. These models must be capable of dealing with the ice induced impulse loads.
Another requirement stated in (DNV, 2013b) is that the vibration calculations shall

be done by solving differential state-equations in the time domain.

2.2 Damping and Hysteresis

Before the model which is used today is explained, some key concepts regarding flexible couplings is explained.

A flexible coupling is often seen as shown in figure 2.7. The FBD shows two masses connected through a flexible element and a damper.

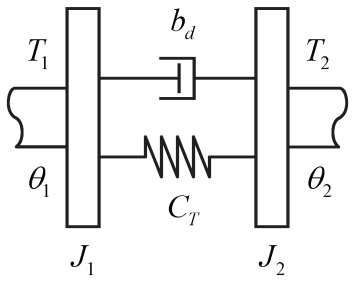

Figure 2.1: Free body diagram of a flexible coupling

The flexible element, or spring, will transfer a torque which depend on how much the two masses are deflected relative to each other. Here this deflection is the difference between the angle θ_1 and θ_2, and is defined as the twist φ. The relation between the flexible torque and the twist is called the spring law:

$$T_{Flex} = K\left(\theta_1 - \theta_2\right) = K\varphi \tag{2.1}$$

Next is the damper. The damper transfers a torque T_{damper} which is expressed using the hydrodynamic damping coefficient b. The hydrodynamic damping coefficient relates the damper torque to the time derivative of the twist, which is the difference between the rotational velocities.

$$T_{Damper} = b\left(\dot{\theta}_1 - \dot{\theta}_2\right) = b\dot{\varphi} \tag{2.2}$$

One of the key concepts when working with damping is hysteresis.
To illustrate this, the damper in figure 2.7 is subjected to a harmonic load. Figure 2.2 shows a time series of the damper twist angle and its time derivative. Since the

excitation is harmonic and the stiffness and damping coefficient is linear, the twist response is harmonic and can be described by equation 2.3

$$\varphi = Acos(\omega_D t) \quad \dot{\varphi} = -\omega_D Asin(\omega_D t) \tag{2.3}$$

A	Deflection amplitude
ω_D	Excitation frequency
φ	Twist angle
τ	Excitation period

The flexible torque and damping torque from equation 2.2 and 2.1 is evaluated for entire loading cycle, from $\varphi(t = 0)$ to $\varphi(t = \tau)$. and plotted against the twist in figure 2.3

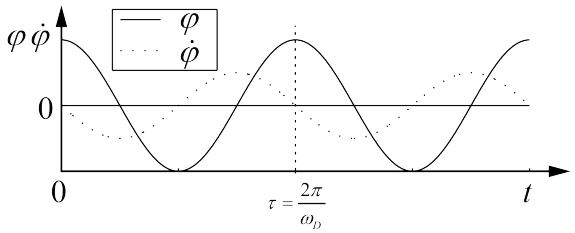

Figure 2.2: Twist angle and its time derivative as a flexible coupling is subjected to a harmonic load.

The work done by twisting the coupling during this period of time is the opposing torque times rotational velocity integrated over the time period. By use of variable change, it can be shown that this is the same as the area under the torque curve when evaluated at different twist angles.

$$W = \int_0^{\tau} T\dot{\varphi}dt = \int_{\varphi(0)}^{\varphi(\tau)} Td\varphi \tag{2.4}$$

W	Energy dissipated during a loading cycle
T	Excitation torque

The flexible torque during one loading cycle shown in figure 2.3 follows the same path as the spring is loaded and unloaded, hence the area enclosed by the curve is equal to zero and no work is done during one cycle. This is since the spring torque acts in the same direction as the twist motion as the spring is unloaded.

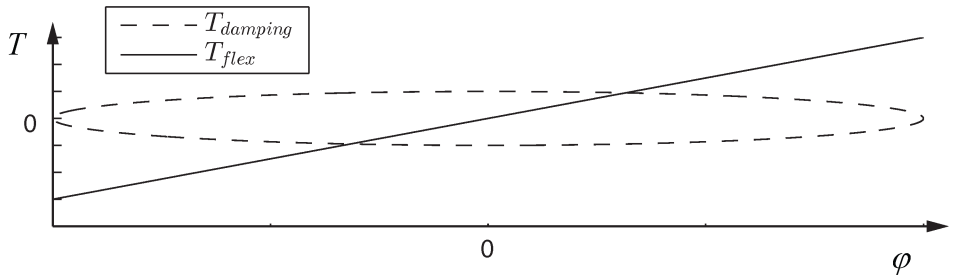

Figure 2.3: Twist torque relation for a damping element, $T_{Damping}$, and a flexible element T_{Flex}.

The damping torque however, does not follow the same path as the damper is unloaded and therefore the area enclosed by the torque graph is not equal to zero and some energy is dissipated during the loading cycle.

The amount of energy dissipated is found by substituting the flexible torque expression equation 2.2 into equation 2.4

$$W = \int_0^\tau b\dot{\varphi}^2 + K\varphi\dot{\varphi}dt \tag{2.5}$$

For the harmonic twist case the work done during one cycle is:

$$W = \int_0^\tau b(\omega_D A sin(\omega_D t))^2 dt = \pi A^2 b\omega_D \tag{2.6}$$

If the flexible torque and damping torque is summed, the result is the hysteresis curve of the flexible coupling which is shown in figure 2.4.

The curve is a useful tool for explaining the behaviour of a damping element and is a part of the documentation required by the DNV GL rules for classiciation (DNV, 2008).

Plotting the hysteresis loop is in addition a way of determining the damping coefficient b. In (DNV, 2008) and in (Pedersen, 2013), is the damping ratio ψ defined as the ratio between the maximum potential energy of the system $U = K\frac{1}{2}\phi_{max}$ and the energy dissipated during one cycle, W.

$$\psi = \frac{W_D}{\frac{1}{2}K\phi_{max}^2} \tag{2.7}$$

By inserting the work done during one cycle and the maximum potential energy for

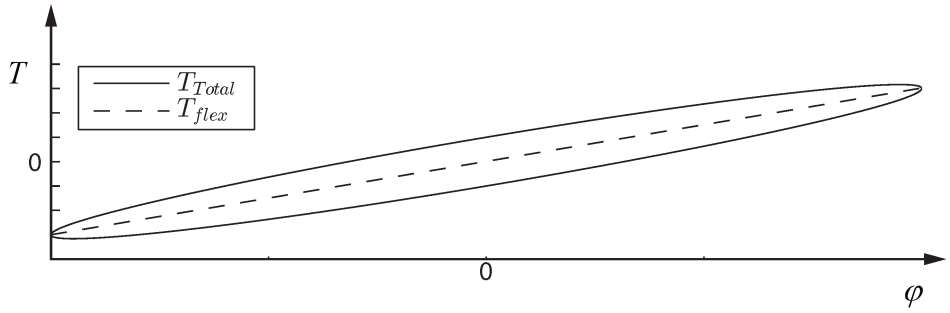

Figure 2.4: Torque twist relation for a flexible coupling

the harmonic twist case, the relation becomes as shown in eq 2.8, and can easily solved for the damping coefficient.

$$\psi = \frac{2\pi b \omega_D}{k} \rightarrow b = \frac{k\psi}{2\pi\omega_D} \tag{2.8}$$

This is useful since the damping coefficient of a damper can be found by plotting the hysteresis loop and evaluating the area of the curve. In the Geislinger coupling catalogue (Geislinger, 2013) is the damping presented using the non dimensional damping factor. This is related to the damping ratio as shown in equation 2.9.

$$\kappa = \frac{\psi}{2\pi} \tag{2.9}$$

In (DNV, 2008) is the rotational stiffness of the coupling defined as:

$$K = \frac{\Delta T_e l}{\Delta\phi} \tag{2.10}$$

Where $\Delta T_e l$ is the difference between the torques at maximum and minimum deflection and $\Delta\phi$ is the difference in maximum and minimum deflection.

2.3 The Geislinger Flexible Coupling

There exist several vibration damper designs in the industry today. However, in this project the focus is on a specific design. Namely the Geislinger damper. A Geislinger damper with major components; inner star, flange, radially aligned springs and intermediate piece, is shown in figure 2.5.

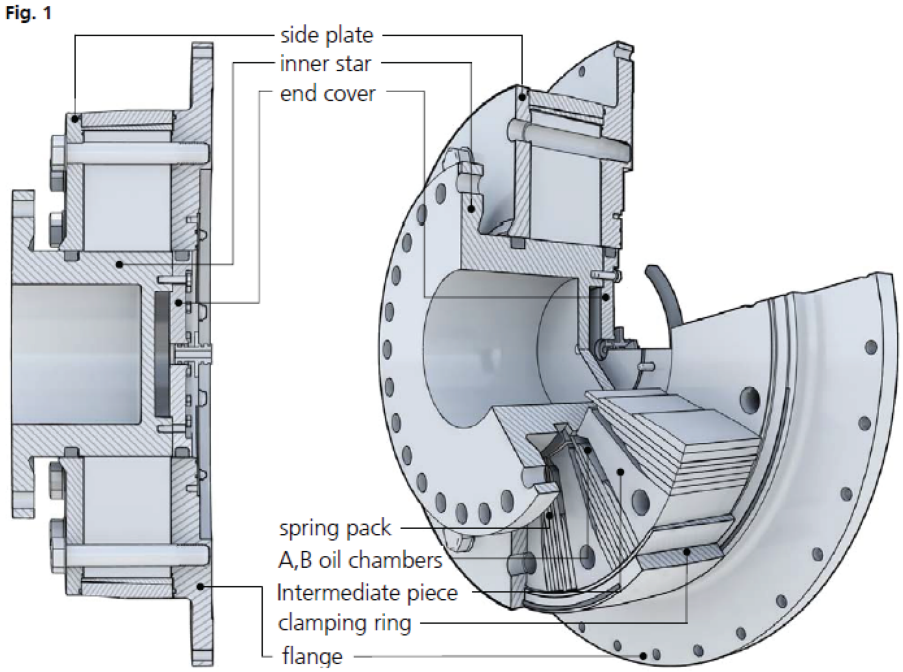

Figure 2.5: Drawing of a Geislinger coupling, naming the major components of the coupling (Geislinger, 2013)

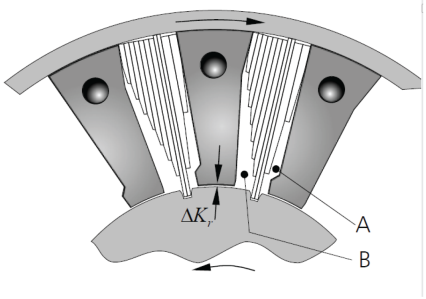

Figure 2.6: Geislinger coupling detail view (Geislinger, 2013)

The springs, inner star and intermediate piece forms cavities which in the Geislinger flexible coupling is oil filled. Figure 2.6 shows a detailed view of the oil chambers and the gap between them.

As the inner star and the flange rotates relative to each other, the springs will have to

deflect. The deflection of the spring causes the volume of oil chamber B to decrease and the volume of oil chamber A to increase, which causes a pressure drop that induced an oil flow from chamber B to chamber A. As the oil flows from chamber B to chamber A through the gap ΔK_r, there is an pressure drop due to the flow resistance over the gap. This flow resistance is the source of the damping in the Geislinger damper.

2.3.1 How the Geislinger damper is modelled today

In (Geislinger, 2013), the manufacturer gives enough data to build a simple damping model shown in figure 2.7. The model consists of the inertia of the inner star, J_I and the inertia of the flange J_F, connected through a damper and a spring. The damping coefficient b_d relates the damping torque to the rotational velocity of the two masses as shown in equation 2.11, while the rotational stiffness relates the flexible torque to the deflection of the flexible coupling as shown in equation 2.12.

$$T_{Damping} = b_d \left(\dot{\theta}_1 - \dot{\theta}_2 \right) \tag{2.11}$$

$$T_{Flex} = C_d \varphi = C_d \left(\theta_1 - \theta_2 \right) \tag{2.12}$$

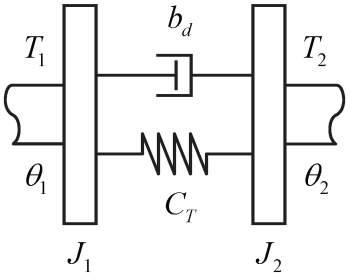

Figure 2.7: FBD of flexible coupling

Further the manufacturer states that they have found the damping coefficient and stiffness values for the damper are found through measurements done on both test rigs and full scale installations using Geislinger couplings. Geislinger also states by using these values, the correct critical speed and loads in every part of the system can be found. The parameters depend on the vibratory frequency ω_D of the damper deflection, where the damper deflection φ, is the difference between θ_1 and θ_2.

Flexible coupling stiffness

How the dynamic torsional stiffness varies with the vibratory frequency of the damper deflection is described by the manufacturer using these equations:

When
$0 \leq \omega \leq \omega_o$

$$C_{Tdyn} = C_{Tstat} \cdot \left(1 + 0.37\frac{\omega_D}{\omega_0}\right) \tag{2.13}$$

When
$\omega_o \leq \omega$

$$C_{Tdyn} = C_{Tstat} \cdot \left(1.1 + 0.27\frac{\omega_D}{\omega_0}\right) \tag{2.14}$$

Where

C_{Tdyn}	–	Dynamic torsional stiffness	$[\mathrm{MN\,m\,rad^{-1}}]$
C_{Tstat}	–	Static torsional stiffness	$[\mathrm{MN\,m\,rad^{-1}}]$
ω_D	–	Vibratory frequency of the damper deflection	$[\mathrm{rad\,s^{-1}}]$
ω_0	–	Characteristic coupling frequency	$[\mathrm{rad\,s^{-1}}]$

The static torsional stiffness is the stiffness experienced when the damper deflection is constant. Since this values does not depend on the magnitude of the deflection, and the fact that the radial spring of the Geislinger coupling has varying cross section, it can be assumed that the value is only valid for small deflections of the damper.

The characteristic coupling frequency is a parameter that relates the damping and dynamic stiffness of the Geislinger coupling to the vibrational frequency. It is a function of the radial clearance ΔK_r and the viscosity of the oil used in the coupling. Both the parameters are given for the individual coupling sizes and designs by the manufacturer.

The dynamic stiffness for vibrational frequencies between 0 $\mathrm{rad\,s^{-1}}$ and 2 times the characteristic coupling frequency is shown in figure 2.8. (Geislinger, 2013) explains that the stiffness increases with frequency due to the displacement of oil, without specifying any further.

Flexible coupling damping

(Geislinger, 2013) describes the damping using the non-dimensional damping factor κ, which is related to the damping coefficient by , b, equation 2.15:

$$b = \frac{\kappa \cdot C_{Tdyn}}{\omega_D} \tag{2.15}$$

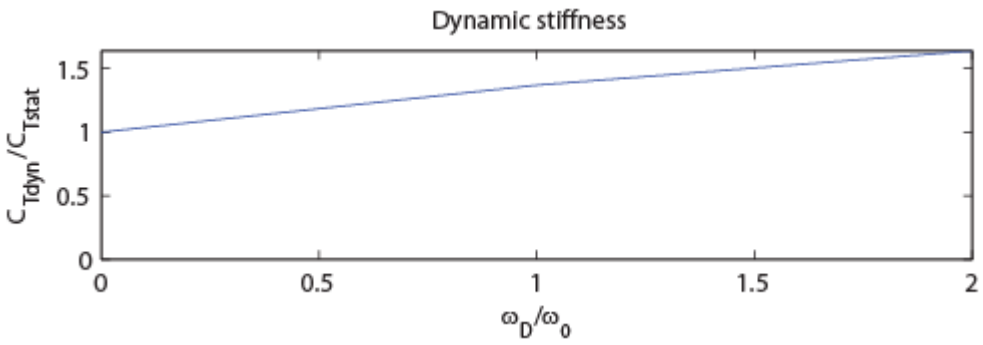

Figure 2.8: Dynamic stiffness of the flexible coupling

For Geislinger couplings with pressurized oil supply, the non-dimensional damping factor is given for different vibrational frequencies by (Geislinger, 2013) as shown in equations 2.16 to 2.18:
When $0 \leq \omega_D \leq 0.3$

$$\kappa = 0.02 + 1.1\frac{\omega_D}{\omega_0} \tag{2.16}$$

When $0.3 \leq \omega_D \leq 1$

$$\kappa = 0.2 + 0.5\frac{\omega_D}{\omega_0} \tag{2.17}$$

When $\omega_D \leq \omega_0$

$$\kappa = 0.7 \tag{2.18}$$

The non dimensional damping factor evaluated at different vibrational frequencies is shown in figure 2.9. Using equation 2.15, the damping coefficient is calculated and shown in 2.10. The damping coefficient decreases with increasing vibratory frequency, and goes to infinity for small vibrational frequencies. The fact that the damping goes to infinity for small values does not make physical sense and might be due to numerical limitations of equation 2.15.

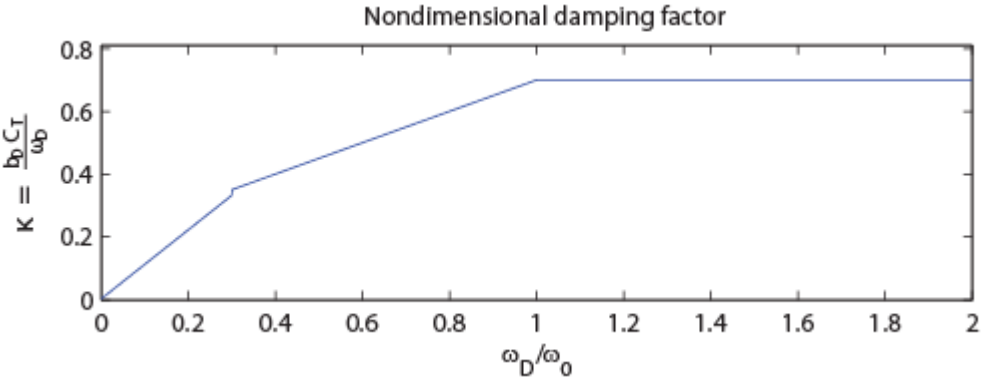

Figure 2.9: Non dimensional damping factor for the flexible coupling

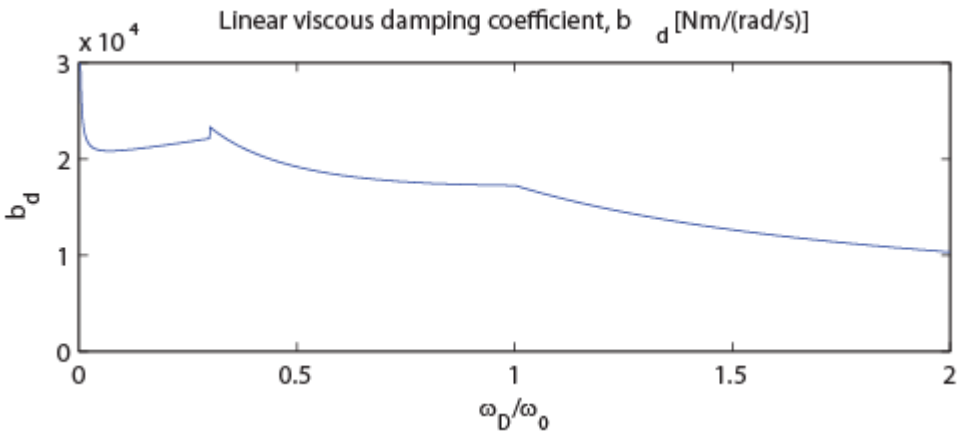

Figure 2.10: Damping coefficient for the flexible coupling

Limitations

In general, it seems that there are several limitations to the modelling procedure presented in citegeislingercoupling that are not mentioned by the manufacturer:

- The vibrational frequency is needed which is not always straight forward to obtain.
- It also demands that the coupling deflection is periodical. This is not the case when the propulsion drive train is subjected to transient loads, e.g. clutch engagement, during ice-propeller interactions
- The static and dynamic stiffness is only valid for small twist angles. How small is not specified by the manufacturer

In addition doesn't the model include the effect of the twist limiter being hit, which is a requirement in (DNV, 2013b)

The flexible coupling with the rest of the propulsion drive train experience both transient loads, and loads that are so large that the twist buffer of the flexible coupling might get hit. In this case will the model presented by Geislinger not be sufficient, and another model capable of incorporating these things will have to be used.

2.4 Ice Propeller Interaction

In his studies (Veitch, 1995) describes the different stages of the propeller interaction by three steps. approach, blockage and contact:

Approach. When ships are operating in ice covered waters, the ship hull tend to break off pieces off ice and submerge them. As the ship advance in the water, the ice pieces are brought in to the vicinity of the propeller, sucked into the propeller and crushed by the propeller blades. According to Veitch, the approach stage begins when the ice piece experiences relative motion between the fluid and the ice piece due to the propeller suction. During this stage, the only effect is the change in hydrodynamic performance of the propeller owing to the change in inflow.

Blockage. The blockage stage starts as the ice piece is in the vicinity of the propeller so that the wake influence on the propeller come to its maximum.

Contact. The contact stage is initiated as the propeller blades comes in direct contact with the ice. In this stage, the forces acting on the propeller are the direct contact forces and hydrodynamic forces.

The problem is describing the forces acting on the propeller. In his Ph.D. Thesis, (Wang, 2007) describes the different loads acting on the propeller blade during ice-propeller interactions: When the ice block blocks the water inflow in front of the propeller, the propeller experience a difference in inflow conditions. corresponding to a lower advance coefficient. This leads to higher thrust and torque coefficients. This is described by Wang as the blockage effect.

Due to the proximity of the ice, the propeller experience unstable inflow conditions and increased gap flow. This results in varying loads and increased risk of cavitation. Wang describes this as the proximity effect. The proximity effect and the blockage effect are referred to as inseparable hydrodynamic loads.

The contact loads depends on different things as described by citeVeitch:95 the ice mechanics, mass and size of the ice, in what way the ice is constrained and the hydrodynamics connected to the ices movement.

In (Wang et al., 2007), the authors mention several complexities present during propeller ice interaction: “ High strain rates, complexity of the flow around the circumference of a propeller, and the randomness in shape and the way of an ice piece interacting with a propeller ”

The ice-propeller interaction process is a complicated phenomenon and there have been done several attempts of describing the physics and making proper mathematical models of the interaction process. Both (Wang et al., 2007) and (Veitch, 1995) recommends that the effects the drive train dynamics has on the ice interaction process is investigated.

2.5 Modelling the ice propeller interaction

The method of describing the ice impact load which is most suitable for the model developed in this project is the method described in (DNV, 2013b) and (Polic et al., 2013).

Depending on the size of the propeller relative to the maximum size of the ice block, the maximum ice-induced torque that arise from the interaction between ice and propeller on one propeller blade is found from the formula:

$$Q_{max} = 10.9 \cdot \left[1 - \frac{d}{D}\right] \cdot \left[\frac{P_{0.7}}{D}\right]^{0.16} \cdot (nD)^{0.17} \cdot D^3 \ \ [kNm] \tag{2.19}$$

$$\text{When } D \leq 1.8 \cdot H_{Ice}$$

$$Q_{max} = 20.7 \cdot \left[1 - \frac{d}{D}\right] \cdot \left[\frac{P_{0.7}}{D}\right]^{0.16} \cdot (nD)^{0.17} \cdot D^{1.9} \cdot H_{Ice}^{1.1} \ \ [kNm] \tag{2.20}$$

$$\text{When } D > 1.8 \cdot H_{Ice}$$

Where

Q_{max}	–	Maximum ice-related torque on a propeller blade	[kNm]
d	–	External diameter of propeller hub	[m]
D	–	Propeller diameter	[m]
$P_{0.7}$	–	Propeller pitch at 0.7 radius	[m]
H_{Ice}	–	Maximum ice block thickness	[m]
n	–	0.85 times the rated engine speed	[RPS]

The torque acting on the propeller shaft as a function of time (or angular position) is according to DNV described as

$$Q(\varphi) = C_q \cdot Q_{Max} \cdot \sin\left(\varphi\left(\frac{180}{\alpha_i}\right)\right) \quad [kNm] \tag{2.21}$$

Where

$Q(\varphi)$	–	Propeller torque	[kNm]
C_q	–	DNV/IACS parameter describing the torque amplitude	[-]
φ	–	Propeller rotational position	[-]
α_i	–	DNV/IACS parameter describing the ice impulse duration	

This is the torque on the propeller shaft from the ice forces acting on one blade. To get the total load on the shaft, the contributions for each of the propellers have to be summed. Between the first blade contact and the last, the number of revolutions is found from:

$$N_Q = 2 \cdot H_{Ice} \tag{2.22}$$

Where N_Q is the number of revolutions during contact

2.6 Oil Compressibility

The specific volume of a fluid is a function of both temperature and pressure. According to (Çengel et al., 2010) is the specific volume of a fluid a function of both pressure and temperature, using tailor series expansion it can be shown that the density can be written as:

$$\rho \approx \rho_0 + \left(\frac{\partial \rho}{\partial T}\right)_{P=const}(T - T_0) + \left(\frac{\partial \rho}{\partial P}\right)_{T=const}(P - P_0) = \rho_0\left(1 + \alpha(T - T_0) + \frac{1}{\beta}(P - P_0)\right) \tag{2.23}$$

Where:

ρ	Fluid density
T	Fluid temperature
P	Fluid pressure
ρ_0	Initial density of the fluid
T_0	Initial temperature of the fluid
P_0	Initial pressure of the fluid

α is defined as the coefficient of volume expansion and shown in equation 2.24. This describes how the density of unit volume of fluid changes with changing temperature and constant pressure.

$$\alpha = \frac{1}{\rho_0}\left(\frac{\partial \rho}{\partial T}\right)_{P=const} \tag{2.24}$$

The bulk modulus of elasticity β, describes how a unit volume of fluid changes density with pressure at constant temperature as shown in equation 2.26. Due to conservation of mass and the fact that Pressure is inversely proportional to volume, the bulk modulus of elasticity can be rewritten as:

$$\beta = \rho_0\left(\frac{\partial P}{\partial \rho}\right)_{T=const} = -V_0\left(\frac{\partial P}{\partial V}\right)_{T=const} \tag{2.25}$$

V Fluid volume
V_0 Initial fluid volume

The bulk modulus is a quantity that changes with pressure as shown in figure 2.11. The gradient of the volume curve decreases with increasing pressure. The bulk modulus is also a function of temperature as it decreases with increasing temperature.

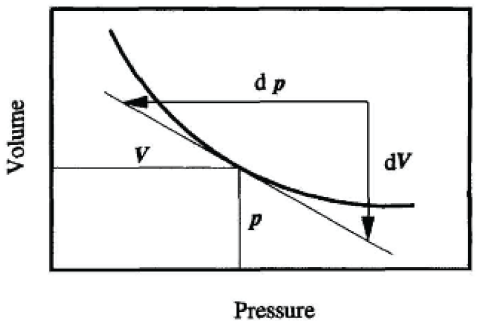

Figure 2.11: Volume change with pressure of a compressible fluid (Hodges, 1996)

The graph above shows how the compressibility of a pure fluid changes with pressure, however in hydraulic appliances such as the flexible coupling will there always be some air present in the fluid. The air trapped in the fluid will have a lower bulk modulus than the fluid and the total bulk modulus of the system will decrease. However at increasing pressure, the volume percent of air present in the fluid will decrease and the effect of the air on the total bulk modulus will decrease. In (Hodges, 1996), the effective compressibility, β_{Eff}, of a hydraulic system containing air is described as:

$$\beta_{Eff} = \Phi_S \beta \tag{2.26}$$

Where Φ is the correction coefficient. It is a function of amount of air present in the hydraulic fluid and the absolute pressure of the system. Figure 2.12 shows how the bulk modulus correction coefficient changes with amount of air in the fluid and the pressure.

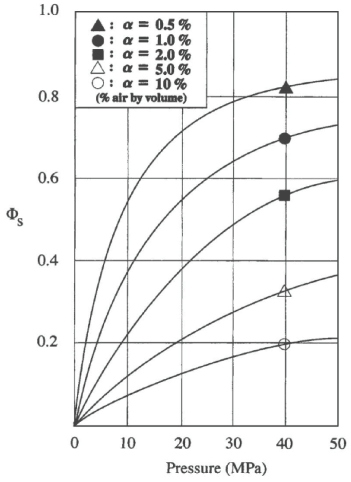

Figure 2.12: Bulk modulus correction coefficient of a fluid containing undissolved air (Hodges, 1996)

Another contribution to the effective bulk modulus of a hydraulic system is the compressibility of the body that contains the fluid. This is especially important in hydraulic appliances where tubes and thin pipes are used. The total effective bulk modulus in a system containing hydraulic fluid, trapped air and flexible boundaries can be compared to a series of springs with the total bulk modulus (or stiffness) as shown in equation 2.27 (McCloy and Martin, 1980).

$$\frac{1}{\beta_{Eff}} = \frac{1}{\beta_{Fluid}} + \frac{1}{\beta_{Boundary}} + \frac{V_{Air}}{V_{Total}} \frac{1}{\beta_{Air}} \tag{2.27}$$

$\frac{V_{Air}}{V_{Total}}$	Volumetric ratio of air present in the total fluid
β_{Fluid}	Bulk modulus of the hydraulic fluid
β_{Air}	Bulk modulus of the Air present in the hydraulic fluid
$\beta_{Boundary}$	Bulk modulus of the body containing the fluid

Chapter 3
Model Development

Geislinger offers a variety of different spring designs, depending on the use of the coupling. Things like if the coupling is going to be reversed, the size of the torque that is going to be transferred , and the required stiffness are things that decide what spring design to use. This project will focus on one of the spring designs, namely the reversible double spring design. In (Geislinger, 2013), the manufacturer presents the spring designs as shown in figure 3.1.

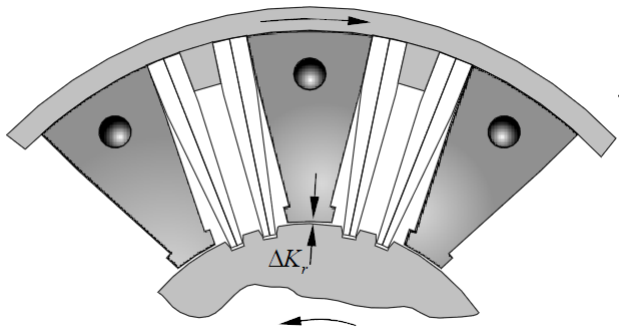

Figure 3.1: Illustration of the dual spring design by (Geislinger, 2013)

What is characteristic for this design is as it name implies that it consists of pairs of springs. The springs are tapered, with the largest cross sectional area towards the outer end of the spring. The stiffness is equal for both positive and negative twist since the tapering is symmetrical about the

3.1 Torque transfer

What is interesting when making a mathematical model of the flexible coupling is the relationship between the torque T_1 and rotational velocity θ_1 at the node on engine side and the effort and flow at the node on the propeller side, T_2 and θ_1.

To find this relationship, the forces that contribute to torque transfer between the two bodies, the inner star and the outer member is considered. The inner star and the outer member are seen as solid bodies, i.e. it has infinite stiffness, and the mass and inertia can be seen as concentrated in two points. The engine side node and propeller side node respectively. The forces that act on the two bodies is in this master thesis divided in to two categories: the forces and moments from the spring acting on the inner and outer member and the oil pressure acting on the oil chamber walls and spring. These forces are indicated in figure 3.2

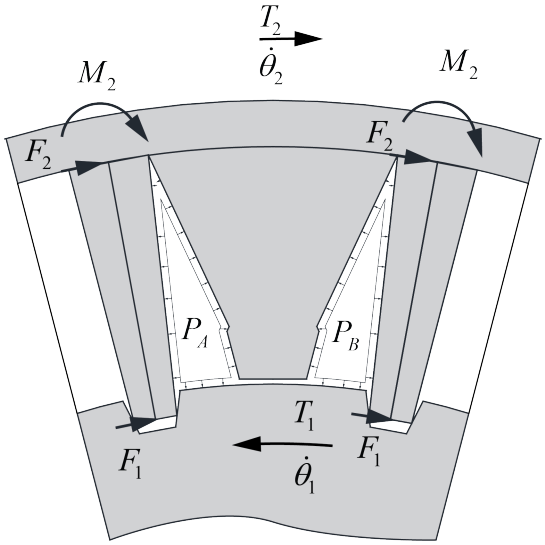

Figure 3.2: Spring support forces and oil pressure acting on the inner and outer member of the coupling.

Where

M_2	Clamping moment between the outer edge of the spring and the outer member
F_1	Tangential contact force between the inner member and the inner edge the spring
F_2	Tangential contact force between the outer member and the outer edge of the spring
T_1	External torque acting on node one (inner member)
T_2	External torque acting on note two (outer member)
$\dot{\theta}_1$	Rotational velocity of node one
$\dot{\theta}_2$	Rotational velocity of node two

Only forces that have tangential components will contribute to the torque transfer, so the size of the tangential component and the distance between its point of attack and the shaft axis determines the size of the torque contribution. Forces that act in other directions might off course affect the size of the torque generating forces, but

this contribution is indirect.

The net tangential pressure force acting on the the oil chamber walls, $\vec{F}_{P-Net}$, is found by evaluating the tangential component of the net pressure force, which is found by integrating the pressure at position $\vec{r}$, and time t, times the tangential vector of the surface $\vec{n}_T$, over the surface S, as shown in equation 3.1

$$\vec{F}_{P-Net}\left(t\right) = \iint_S p\left(\vec{r},t\right)\vec{n}\ dS \tag{3.1}$$

The pressure distribution is however simplified so that the pressure is constant throughout the chamber volume. This simplification means that the net force pressure force is simply the pressure at time t, times the surface area of the wall:

$$\vec{F}_{P-Net}\left(t\right) = p\left(t\right)\iint_S \vec{n}\ dS = p\left(t\right)A_S \tag{3.2}$$

Since we are only interested in the tangential component of the pressure force, only the tangential component n_T of the normal vector is used and equation 3.2 becomes as shown in equation 3.3, where A_T is the tangential projection of the wall surface.

$$F_P\left(t\right) = p\left(t\right)\iint_S n_T\ dS = p\left(t\right)A_T \tag{3.3}$$

The only surfaces that have tangential projections is the spring surfaces and surface A and B. Since the oil chambers are symmetrical is the tangential projection of the inner oil chamber found from equation 3.4.

$$A_T = (r_2 - r_2)w_{Chamber} \tag{3.4}$$

Where r_2 and r_1 is the distance between the inner and outer chamber wall and the coupling axis as shown in figure 3.3, and $w_{Chamber}$ is the width of the oil chamber. The torque generating force acting on surface A and B, F_A and F_B is then found from equation 3.5.

$$F_B = p_B(t)A_T \quad , \quad F_A = p_A(t)A_T \tag{3.5}$$

Where $p_A(t)$ and $p_B(t)$ is the pressure in chamber A and B.

The pressure that acts on the spring force is included in the spring force and is discussed further in section 3.3.

The spring is seen as simply supported at the end facing the inner star and fixed relative to the outer member, in addition is the maximum deflection of the coupling small

so any radial component of the force transmitted by the spring is neglected.

Assuming this is the supporting force at the inner and outer end of the spring F_1 and F_2 in addition to the clamping moment at the outer end M_2, the direct contributions from the spring to the torque transfer between the inner and outer member.

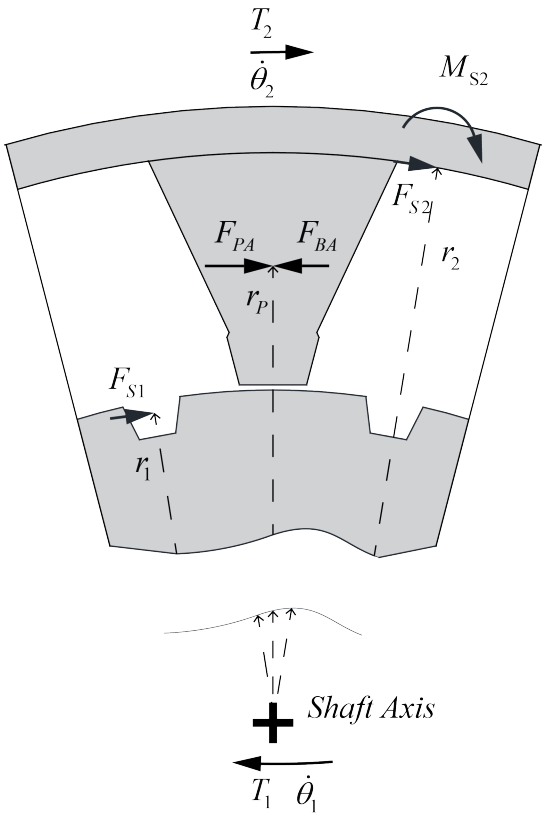

Figure 3.3: The forces acting on the inner and outer member of the coupling producing torque

The torque generated by these forces is found by multiplying the size of the force by the distance between its point of attack and the shaft axis. The distances are indicated in figure 3.3.

The global coupling relations is then found by summing the external torques acting on the nodes T_1 and T_2 with the torques from the spring and the oil pressure, in addition to the inertia of the inner and outer member as shown in equation 3.6. The sign convention is defined from figure 3.3. Since there are several chamber and spring pairs (or cells) and these are assumed to deform uniformly is the torque acting on one cell the total nodal torque divided by the number of cells n_{cells}.

$$\begin{array}{ll} \frac{T_1}{n_{cell}} & = F_1 r_1 + J_1 \ddot{\theta}_1 \\ \frac{T_1}{n_{cell}} & = -\left(F_B - F_A\right) r_P - F_2 r_2 - J_2 \ddot{\theta}_2 - M_2 \end{array} \tag{3.6}$$

Multiplying the equations above with the appropriate rotational velocities of the nodes, $\dot{\theta}_1$ and $\dot{\theta}2$, yields the power relations of the inner and outer members. This power relation corresponds to the bond graph relation shown in figure 3.4

$$\begin{array}{ll} \dot{\theta}_1 T_1 & = \dot{\theta}_1 F_1 r_1 + \dot{\theta}_1 J_1 \ddot{\theta}_1 \\ \dot{\theta}_2 T_2 & = -\dot{\theta}_2 \left(F_B - F_A\right) r_P - \dot{\theta}_2 F_2 r_2 - \dot{\theta}_2 J_2 \ddot{\theta}_2 - \dot{\theta}_2 M_2 \end{array} \tag{3.7}$$

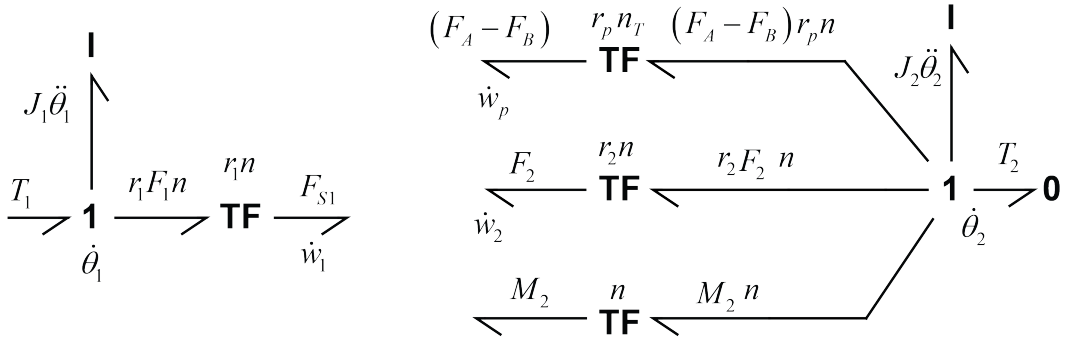

Figure 3.4: Global power bond relations of the flexible coupling. The inner and outer member are not connected.

Next these are the torques acting on the nodes related to each other, starting with the torques from the oil hydrodynamics before we continue with the spring dynamics.

3.2 Modelling the spring

The spring model is developed based on the method for modelling lumped models of continua through separation of variables presented in (Karnopp et al., 2012a). Which is a approximation method for solving the the Euler Bernoulli beam equation of motion (equation 3.8), using a finite number of flexible modes.

To model the spring, the free free boundary conditions are used. This is since both the inner star and outer member rotate. As shown in equation 3.8 and figure 3.5, there is a force and torque, F_1 and M_1, acting on the beam at position 1 and a force and torque,F_2 and M_2, acting on the beam at position 2. These forces and torques represents the boundary conditions

Want to solve the beam equation by using separation of variables.

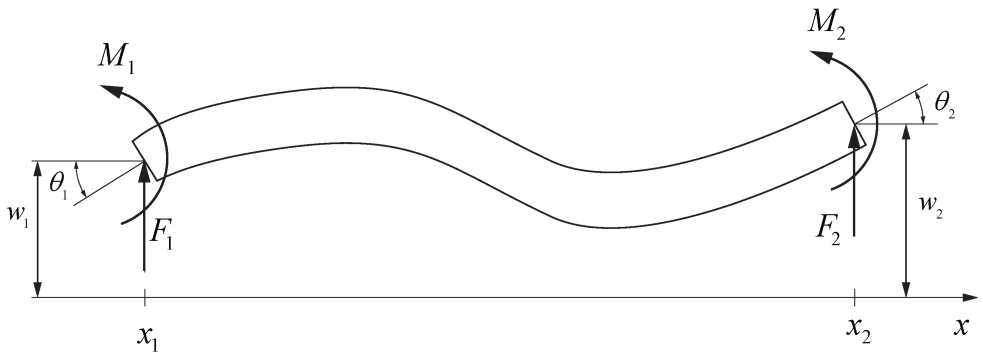

Figure 3.5: Torques, Forces, rotation and translation of a free-free beam

$$\begin{aligned} EI\frac{\partial^4 w}{\partial x^4} + \rho A\frac{\partial^2 w}{\partial x^2} =& F_1\delta(x-x_1) + \frac{\partial^2(M_1\partial(x-x_1))}{\partial x^2} \\ &+ F_2\delta(x-x_2) + \frac{\partial^2(M_2\partial(x-x_2))}{\partial x^2} \end{aligned} \tag{3.8}$$

E	Young Modulus for spring material
I	Area Inertia of the spring profile
ρ	Density of the spring material
A	Area of the spring profile
x	Position along the spring
w	Spring deflection
$\delta(x-x_1)$	Diracs Delta function
$F1$	External force acting at position x_1
$F2$	External force acting at position x_2
$M1$	External torque acting at position x_1
$M2$	External torque acting at position x_2

3.2.1 solving the homogenous differential equation

To solve the beam equation of motion by separation of variables, the mode shapes and Eigen frequencies are needed. These are found by first solving the homogeneous differential equation 3.9.

$$EI\frac{\partial^4 w}{\partial x^4} + \rho A\frac{\partial^2 w}{\partial x^2} = 0 \tag{3.9}$$

To do this, it is assumed that the deflection can be described as the product of a function of time,$f(t)$ and a function of position,$Y(x)$,.

$$w(x,t) = Y(x)f(t) \tag{3.10}$$

In addition, by convention is,ω (omega) defined by $f(t)$ as shown in equation 3.11. Next k is defined in equation 3.12.

$$\omega^2 = -\frac{1}{f}\frac{d^2f}{dt^2} \tag{3.11}$$

$$k^4 = \frac{\rho A}{EI}\omega^2 \tag{3.12}$$

Substituting the definition of k and ω in addition to the deflection as shown in equation 3.10, into the beam equation, the result is a differential equation with Y as the variable.

$$\frac{d^4Y}{dx} - k^4Y = 0 \tag{3.13}$$

For flexible modes, this differential equation is assumed to have the general solution shown in equation 3.14.

$$Y(x) = A\cosh(kx) + B\sinh(kx) + C\cos(kx) + D\cos(kx) \tag{3.14}$$

The constants A, B, C, D and k in the assumed solution is found by using the force and moment free boundary conditions:

$$\frac{d^2w}{dx^2}(x=0) = \frac{d^2w}{dx^2}(x=L) = 0 \tag{3.15}$$

$$\frac{d^3w}{dx^3}(x=0) = \frac{d^3w}{dx^3}(x=L) = 0 \tag{3.16}$$

Where L is the length of the spring.
Using equation 3.10, the boundary conditions can be rewritten to:

$$\frac{d^2Y}{dx^2}(x=0) = \frac{d^2Y}{dx^2}(x=L) = 0 \tag{3.17}$$

$$\frac{d^3Y}{dx^3}(x=0) = \frac{d^3Y}{dx^3}(x=L) = 0 \tag{3.18}$$

For the solution to satisfy the boundary conditions, the solution must also satisfy the frequency equation 3.19.

$$\cosh(kL)\cos(k_nL) = 1 \tag{3.19}$$

This equation has several solutions for k, and must be found numerically. The equation has n solutions where $k_n = 0$ is one.

When k_n is found, the Eigenfrequencies can be found from equation 3.11.
One solution to the beam equation of motion that satisfies both the frequency equation and the boundary conditions is shown in equation 3.20.

$$Y_n = \sin(k_n x) + \sinh(k_n x) + \left(\frac{\sinh(k_n L) - \sin(k_n L)}{\cos(k_n L) - \cosh(k_n L)}\right)(\cos(k_n x) + \cosh(k_n x)) \quad (3.20)$$

This is also satisfied by the two solid body modes, which describes translation and rotation.

$$Y_{00} = 1 \quad (3.21)$$

$$Y_0 = x - \frac{L}{2} \quad (3.22)$$

3.2.2 Finding the forced response

To find the forced response it is assumed that the response can be represented by a weighted sum of n natural modes:

$$w(x,t) = \sum_{n=0}^{\infty} Y_n(x)\eta_n(t) \quad (3.23)$$

This sum is then substituted into the forced equation of motion 3.8. Next, each side of the equation is multiplied by an arbitrary mode shape, denoted m, and integrated over the length of the spring, which yield:

$$\int_0^L \sum_{n=0}^{\infty} \rho A \omega_n^2 Y_m Y_n \eta_n(t) dx + \int_0^L \sum_{n=0}^{\infty} \rho A Y_m Y_n \ddot{\eta} dx =$$
$$\int_0^L Y_m(x)\left(F_1\delta(x-x_1) + \frac{\partial^2(M_1\partial(x-x_1))}{\partial x^2} + F_2\delta(x-x_1) + \frac{\partial^2(M_2\partial(x-x_1))}{\partial x^2}\right)dx \quad (3.24)$$

Due to the orthogonality of the mode shapes, the only contribution from the summation is the n=m mode. In other words, terms including the product of a mode shape and any other mode shape than itself is zero. Next step is defining the modal mass and modal stiffness as in equations 3.25 and 3.26. Now the left hand side of equation 3.24 can be written as equation 3.27:

$$m_n = \int_0^L \rho A {Y_n}^2 dx \tag{3.25}$$

$$k_n = m_n {\omega_n}^2 \tag{3.26}$$

$$\int_0^L \sum_{n=0}^{\infty} \rho A \omega_n^2 {Y_m}^2 \eta_n dx + \int_0^L \sum_{n=0}^{\infty} \rho A {Y_m}^2 \ddot{\eta} dx = k_n \eta_n(t) + m_n \ddot{\eta}_n \tag{3.27}$$

Since the area between Dirac's delta function and the x axis is equal to one, the right hand side of equation 3.24 can be written as:

$$\begin{aligned} \int_0^L Y_m(x) \left(F_1 \delta(x - x_1) + \frac{\partial^2 (M_1 \partial(x - x_1))}{\partial x^2} + F_2 \delta(x - x_1) + \frac{\partial^2 (M_2 \partial(x - x_1))}{\partial x^2} \right) dx \\ = Y_n(x_1) F_1 + \frac{dY_n}{dx}(x_1) M_1 + Y_n(x_2) F_2 + \frac{dY_n}{dx}(x_2) M_2 \end{aligned} \tag{3.28}$$

The result is the modal equation of motion:

$$k_n \eta_n + m_n \ddot{\eta}_n = Y_n(x_1) F_1 + \frac{dY_n}{dx}(x_1) M_1 + Y_n(x_2) F_2 + \frac{dY_n}{dx}(x_2) M_2 \tag{3.29}$$

The modal equations of motion for n modes can be written on matrix form:

$$[M] \, \overrightarrow{\ddot{\eta}} + [K] \, \overrightarrow{\eta} = [r_1] \, \overrightarrow{F} \tag{3.30}$$

Where the parameter matrices are

$$[M] = \begin{bmatrix} m_1 & 0 & \cdots & 0 \\ 0 & m_2 & \cdots & 0 \\ \vdots & \vdots & \ddots & \vdots \\ 0 & 0 & \cdots & m_n \end{bmatrix} \tag{3.31}$$

$$[K] = \begin{bmatrix} k_1 & 0 & \cdots & 0 \\ 0 & k_2 & \cdots & 0 \\ \vdots & \vdots & \ddots & \vdots \\ 0 & 0 & \cdots & k_n \end{bmatrix} \tag{3.32}$$

$$[r_1] = \begin{bmatrix} Y_1(x_1) & \frac{\partial}{\partial x} Y_1(x_1) & Y_1(x_2) & \frac{\partial}{\partial x} Y_1(x_2) \\ Y_2(x_1) & \frac{\partial}{\partial x} Y_2(x_1) & Y_2(x_2) & \frac{\partial}{\partial x} Y_2(x_2) \\ \vdots & \vdots & \vdots & \vdots \\ Y_n(x_1) & \frac{\partial}{\partial x} Y_n(x_1) & Y_n(x_2) & \frac{\partial}{\partial x} Y_n(x_2) \end{bmatrix} \tag{3.33}$$

And the modal displacement, modal acceleration and force vectors are respectively:

$$\overrightarrow{\eta} = \begin{bmatrix} \eta_1 \\ \eta_2 \\ \vdots \\ \eta_n \end{bmatrix} \quad (3.34) \qquad \overrightarrow{\ddot{\eta}} = \begin{bmatrix} \ddot{\eta}_1 \\ \ddot{\eta}_2 \\ \vdots \\ \ddot{\eta}_n \end{bmatrix} \quad (3.35) \qquad \overrightarrow{F} = \begin{bmatrix} F_1 \\ M_1 \\ F_2 \\ M_2 \end{bmatrix} \quad (3.36)$$

The modal equation of motion, eq 3.29, states that the sum of the modal inertia force and modal stiffness force is equal to the modal excitation force, with the time derivative of the modal displacement as the common flow variable.

In bond graph notation, this summation of efforts is done in the 1-junction as shown in figure 3.6.

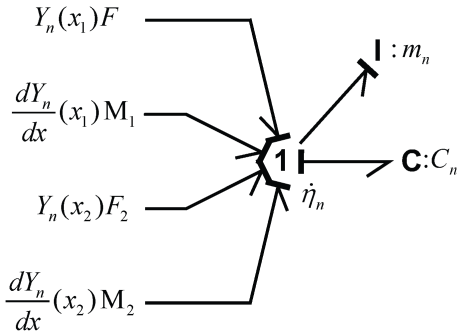

Figure 3.6: Bond graph representation of the modal equation of motion

As previously mentioned, the displacement at any point can be found from equation 3.23. Taking the time derivative of this equation gives the relationship between the deflection velocity and the n-number of modal velocities.

$$\dot{w}(x) = \sum_{n=0}^{\infty} Y_n(x)\dot{\eta}_n \quad (3.37)$$

This summation of flows is shown using bond graph notation in figure 3.7.
The same can be done for the beam slope and its time derivative, using the mode slope, instead of the mode shape.

$$\dot{\theta}(x) = \sum_{n=0}^{\infty} \frac{dY_n(x)}{dx}\dot{\eta}_n \quad (3.38)$$

Combining figure 3.6, 3.7 and 3.8 for two modes is shown in figure 3.9.

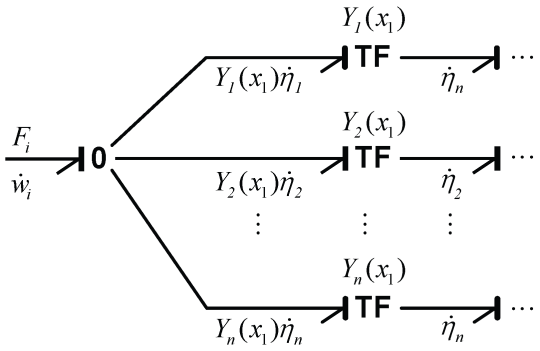

Figure 3.7: Bond graph representation of the spring deflection velocity found as a weighted sum of mode shapes

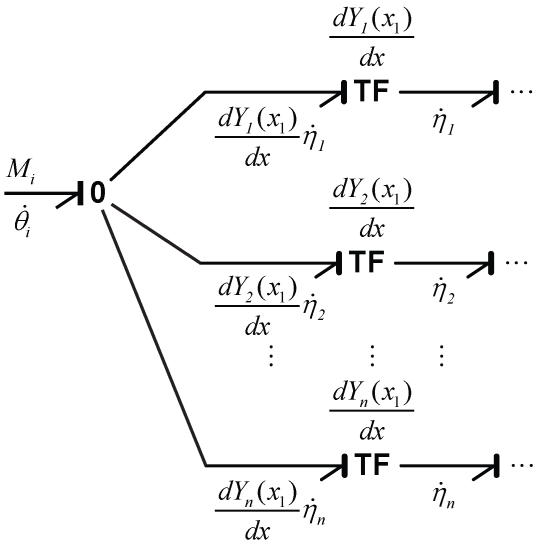

Figure 3.8: Bond graph representation of the spring deflection slope velocity found as a weighted sum of mode shapes

In this figure only two modes are included. If more modes were to be included they would be added to the zero junctions. If more modes were to be included, the model would become messy. Therefore the field bond graph notation will be used further.

Developing the field bond graph is straight forward using equation 3.31. One challenge is however that due to the two zero frequency modes, the K-matrix has elements that are zero along the diagonal, which makes it impossible to invert. To avoid this, the K

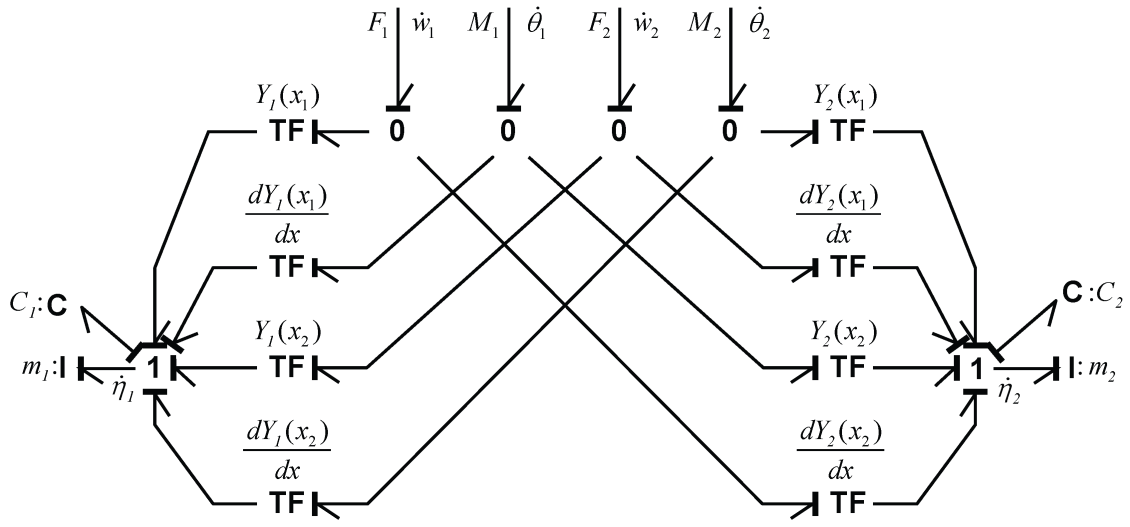

Figure 3.9: Scalar bond graph representation of the spring including two modes.

matrix is reduced to a n-2 by n-2 matrix, omitting the two zero frequency modes. The vector power bond is reduced using a TF-element with the relation shown in equation 3.40 (the subscript denotes the matrix dimension).

$$\vec{\eta}_{[n-2]} = [r_2]_{n\times(n-2)}\vec{\eta}_{[n]} \tag{3.39}$$

$$\begin{bmatrix} \dot{\eta}_3 \\ \dot{\eta}_4 \\ \vdots \\ \dot{\eta}_n \end{bmatrix} = \begin{bmatrix} 0 & 0 & 1 & 0 & \cdots & 0 \\ 0 & 0 & 0 & 1 & \cdots & 0 \\ \vdots & \vdots & \vdots & \vdots & \ddots & 0 \\ 0 & 0 & 0 & 0 & 0 & 1 \end{bmatrix} \begin{bmatrix} \dot{\eta}_1 \\ \dot{\eta}_2 \\ \dot{\eta}_3 \\ \dot{\eta}_4 \\ \vdots \\ \dot{\eta}_n \end{bmatrix} \tag{3.40}$$

The field bond graph representation of the finite mode distributed parameter model of the spring is shown in figure 3.10

The bond graph model, shown in figure 3.10, only give the spring deflection at the boundaries. To find the volume of the Geislinger damper oil chambers, the deflection along the length of the spring is needed. As stated in (Karnopp et al., 2012a): "... Any location on the rod can be used as an output. We simply consider any desired output point as a location for a force input equal to zero"

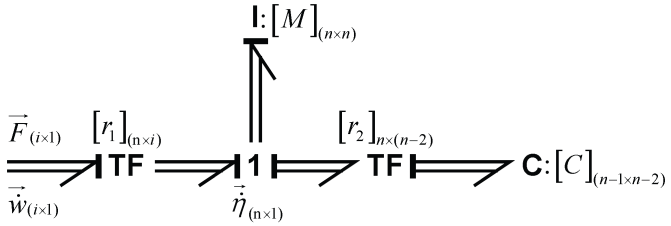

Figure 3.10: Field bond graph representation of the spring including n modes and i output positions

In this model, this is done by increasing the number of excitation forces and moments, i, acting on the spring and letting them act evenly distributed over the spring as shown in figure 3.11.

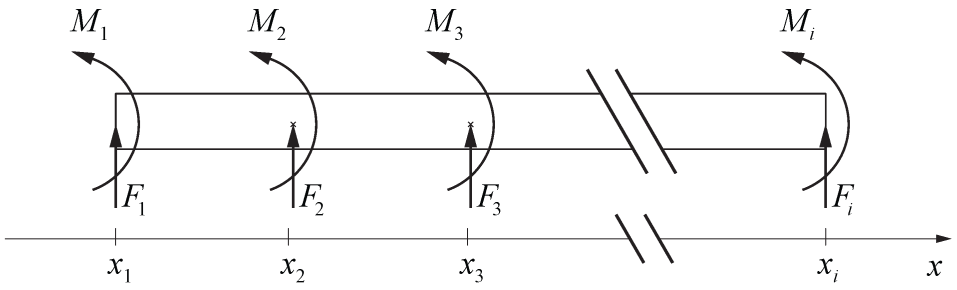

Figure 3.11: Spring with evenly distributed output positions

For i output positions, the n by $2i$,r1 matrix relating the modal velocities and deflection velocities is shown in equation 3.41. The second dimension of the matrix is $2i$ since both the mode shape and mode shape slope evaluated at the i positions is needed.

$$[r_1] = \begin{bmatrix} Y_1(x_1) & \frac{\partial}{\partial x}Y_1(x_1) & Y_1(x_2) & \frac{\partial}{\partial x}Y_1(x_2) & \cdots & Y_1(x_i) & \frac{\partial}{\partial x}Y_1(x_i) \\ Y_2(x_1) & \frac{\partial}{\partial x}Y_2(x_1) & Y_2(x_2) & \frac{\partial}{\partial x}Y_2(x_2) & \cdots & Y_2(x_i) & \frac{\partial}{\partial x}Y_2(x_i) \\ \vdots & \vdots & \vdots & \vdots & \cdots & \vdots & \vdots \\ Y_n(x_1) & \frac{\partial}{\partial x}Y_n(x_1) & Y_n(x_2) & \frac{\partial}{\partial x}Y_n(x_2) & \cdots & Y_n(x_i) & \frac{\partial}{\partial x}Y_n(x_i) \end{bmatrix} \tag{3.41}$$

3.2.3 Damping

As with most physical motion, there is loss associated with the spring response. The loss, or damping, is in reality spatially distributed, similar to the spring stiffness and inertia mass. Including damping in the same way as stiffness and inertia is however difficult. As stated in (Borutzky, 2010), "...the well known separation-of-variables approach, in general, is only applicable it there is no damping term in the differential equation.". further states that it is possible to obtain useful results by including damping to each mode using a resistor with linear damping coefficient. According to (Karnopp et al., 2012a) and (Borutzky, 2010), the linear modal damping coefficient is presented as shown in equation 3.42, a function of the modal mass, the Eigen frequency and the modal damping ratio. The mentioned modal damping ratio is usually found experimentally.

$$b_n = 2\xi_n \omega_n m_n \tag{3.42}$$

Where:

b_n	Modal damping coefficient
ξ_n	Modal damping ratio
ω_n	Natural frequency of the mode
m_n	Modal mass

The modal equation of motion including damping, is shown in equation 3.43, and the corresponding bond graph model is shown in figure 3.12, with the modal damping matrix as shown in equation 3.44.

$$k_n\eta_n + b_n\dot{\eta} + m_n\ddot{\eta}_n = Y_n(x_1)F_1 + \frac{dY_n}{dx}(x_1)M_1 + Y_n(x_2)F_2 + \frac{dY_n}{dx}(x_2)M_2 \tag{3.43}$$

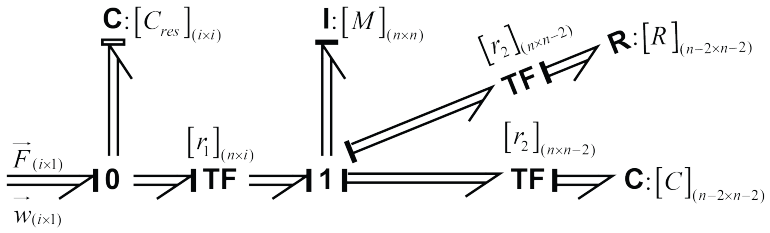

Figure 3.12: Field bond graph representation of the spring including n modes and i output positions

$$[R] = \begin{bmatrix} b_1 & 0 & \cdots & 0 \\ 0 & b_2 & \cdots & 0 \\ \vdots & \vdots & \ddots & \vdots \\ 0 & 0 & \cdots & b_n \end{bmatrix} \tag{3.44}$$

3.2.4 Residual compliance

As explained in (Borutzky, 2010) and (Karnopp et al., 2012a), is only a finite number of modes needed to give correct response at a given frequency range. The numbers of modes should be between 2 and 5 times the maximum frequency experienced. The reason for this is that below a natural frequency, it is only the stiffness of the mode that contribute to the response. The mass and damping does not.
By solving the modal equation of motion it can be shown that the modal displacement for high values of ω_n can be simplified to:

$$\eta_n = C_n \left(Y_n(x_1) \cdot F_1 + \frac{dY_n(x_1)}{dx} \cdot M_1 + Y_n(x_2) \cdot F_2 + \frac{dY_n(x_2)}{dx} \cdot M_2 \right) \tag{3.45}$$

In (Borutzky, 2010) and (Karnopp et al., 2012a) it is shown how the residual compliance of a element can be developed. This is done for the radial springs next
The number of modes at which inertia damping and stiffness is included is from now on reffered to as n. The compliance terms of the remaining modes, from mode $n+1$ to ∞ , defined as the residual compliance, is developed next.

The beam displacement w found as a weighted sum of mode shapes and modal displacements shown in equation 3.23, can be split into two parts as shown in equation 3.46. Here w' is including modes 1 to n, and w_{res} includes the modes from $n+1$ and up.

$$w(x_i, t) = w'(x_i, t) + w_{res}(x_i, t) \tag{3.46}$$

$$w'(x_i, t) = \sum_{v=0}^{n} Y_v(x_i)\eta_v \tag{3.47}$$

$$w(x_i, t)_{res} = \sum_{v=n+1}^{\infty} Y_v(x_i)\eta_v \tag{3.48}$$

Substituting the modal displacement from equation 3.45 into the residual deflection expression 3.48 gives the expression for the residual compliance shown in equation 3.49.

$$w(x_i,t)_{res} = \sum_{v=n+1}^{\infty} Y_v(x_i)C_v \left(Y_v(x_1)\cdot F_1 + \frac{dY_v(x_1)}{dx}\cdot M_1 + Y_v(x_2)\cdot F_2 + \frac{dY_v(x_2)}{dx}\cdot M_2 \right) \tag{3.49}$$

Expanding the residual deflection to include the deflection and rotation at i positions the expression becomes as shown in equation 3.50 with the residual compliance matrix defined from equation 3.51

$$\overrightarrow{w}_{res} = [r_{1,res}]^T [C] [r_{1,res}] \overrightarrow{F}_i = [C_{res}] \overrightarrow{F}_i \tag{3.50}$$

$$\overrightarrow{w_{res}} = \begin{bmatrix} w_{1,res} \\ \theta_{1,res} \\ w_{2,res} \\ \theta_{2,res} \\ \vdots \\ w_{i,res} \\ \theta_{i,res} \end{bmatrix} \tag{3.51}$$

$$[C_{res}] = [r_{1,res}]^T [C] [r_{1,res}] = \begin{bmatrix} C_{n+1} & 0 & \cdots & 0 \\ 0 & C_{n+2} & \cdots & 0 \\ \vdots & \vdots & \ddots & \vdots \\ 0 & 0 & \cdots & C_v \end{bmatrix} \tag{3.52}$$

$$[r_{1,res}] = \begin{bmatrix} Y_{n+1}(x_1) & \frac{\partial}{\partial x}Y_{n+1}(x_1) & Y_{n+1}(x_2) & \frac{\partial}{\partial x}Y_{n+1}(x_2) & \cdots & Y_{n+1}(x_i) & \frac{\partial}{\partial x}Y_{n+1}(x_i) \\ Y_{n+2}(x_1) & \frac{\partial}{\partial x}Y_{n+2}(x_1) & Y_{n+2}(x_2) & \frac{\partial}{\partial x}Y_{n+2}(x_2) & \cdots & Y_{n+2}(x_i) & \frac{\partial}{\partial x}Y_{n+2}(x_i) \\ \vdots & \vdots & \vdots & \vdots & \cdots & \vdots & \vdots \\ Y_v(x_1) & \frac{\partial}{\partial x}Y_v(x_1) & Y_v(x_2) & \frac{\partial}{\partial x}Y_v(x_2) & \cdots & Y_v(x_i) & \frac{\partial}{\partial x}Y_v(x_i) \end{bmatrix} \tag{3.53}$$

Here, the $[r_{1,res}]$ and $[C]$ matrices are the same as the ones described in the previous section , only now they include modes n+1 and upwards. The residual compliance matrix is an i by i matrix, relating efforts and displacements, which corresponds to a C-field. The summation of the displacements in equation 3.46 is taken care of by a 0 junction and the resulting bond graph is shown in figure 3.13.

The advantage of including the residual compliance as a sum of the contributions from the v modes, is that the sum converges after relatively few modes, and a finite amount of modes is needed for a residual compliance matrix with satisfying accuracy. This is since the modal compliance decrease at higher modes and the high order modes contribution to the sum is eventually of no significance.

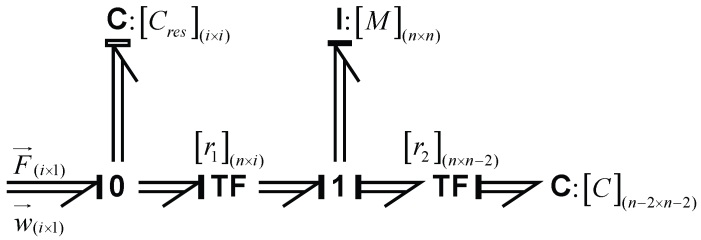

Figure 3.13: Finite mode field bond graph representation of the spring, including residual compliance

3.3 Modelling the oil flow

The hydraulic part of the coupling is modelled using the procedure described in Pedersen and Engja (2008)

The hydraulic system is divided in to two control volumes Chamber A, chamber B with the slit K_{Slit} combining them as shown in figure 3.14.

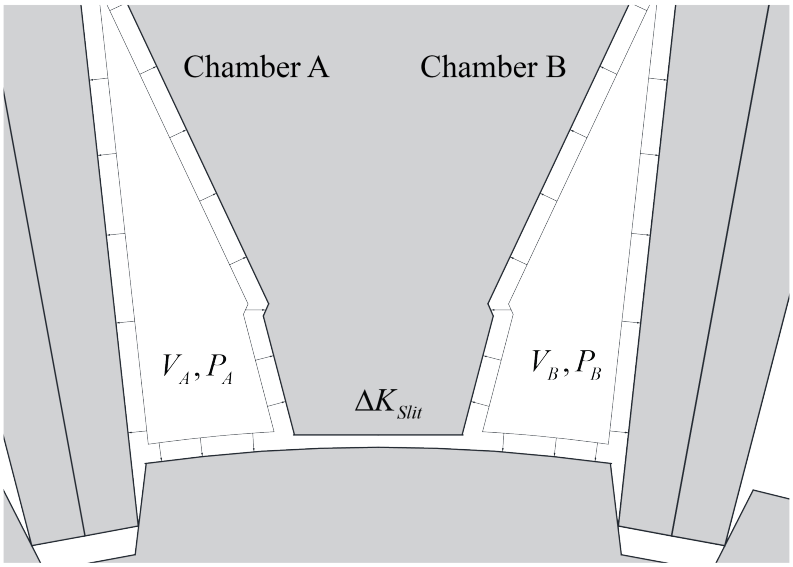

Figure 3.14: Oil chambers A and B

As the inner and outer member rotate, will both the control volume surface facing the spring A_{Spring} and the control volume facing the inner wall A_t move causing the control volume change. In addition there will be fluid flow through the slit K_{Slit} and change

of fluid volume due to the compressibility of the fluid. The relationship between the volume change rates is shown in equation 3.54.

$$\begin{aligned} \Delta Q_A &= Q_{Aspring} - Q_{AT} - Q_{Slit} \\ \Delta Q_B &= Q_{Slit} + Q_{AT} - Q_{Bspring} \end{aligned} \tag{3.54}$$

Where:

ΔQ_A	Rate of fluid compression in chamber A
ΔQ_B	Rate of fluid compression in chamber A
$Q_{Aspring}$	Volume change rate due to the moving spring in chamber A
$Q_{Bspring}$	Volume change rate due to the moving spring in chamber B
Q_{AT}	Volume change rate due to the moving inner wall
Q_{Slit}	Volume flow through the slit

The pressure in chamber A and B, which is assumed to be constant throughout the chamber volumes is defined as P_A and P_B. By multiplying equation 3.54 by the appropriate pressures the result is the energy change rate of the control volumes. This relation corresponds to 0-junctions as shown in figure 3.16

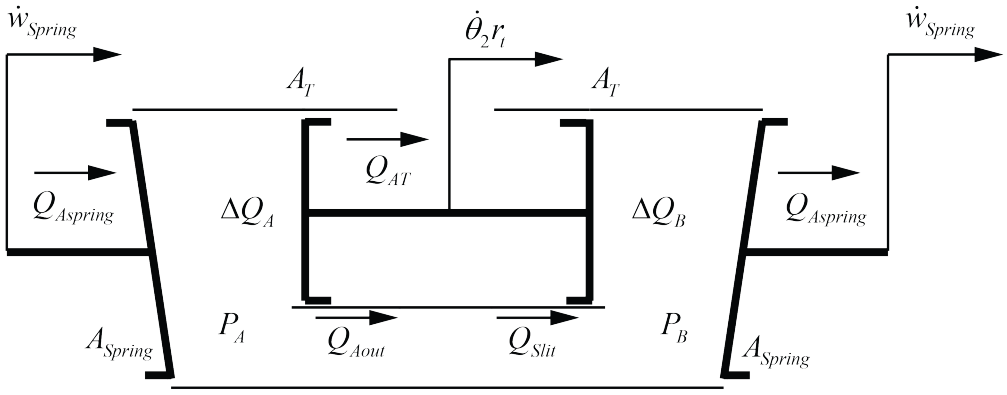

Figure 3.15: FBD of hydraulic part of the geislinger coupling

Fluid compressibility

The bulk modulus of the system is as explained in section 2.6 dependent on the temperature of the system, the amount of trapped air in the system and the stiffness of the body containing the hydraulic fluid. The effect of air in the system is neglected, and the stiffness of the flexible coupling is seen as large compared to the bulk modulus of the fluid, so only the effect bulk modulus of the hydraulic fluid is included.

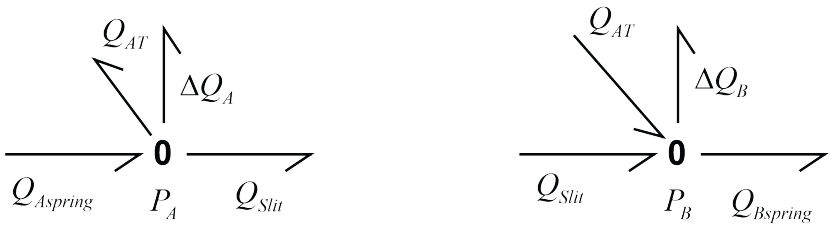

Figure 3.16: Summation of flows to and from the oil chambers

The compressibility is included using the finite difference form of the bulk modulus as explained in in (Pedersen and Engja, 2008), where the bulk modulus is defined as the pressure change due to compression of a fluid volume:

$$\beta = -V_{CV}\frac{\Delta P}{\Delta V} \tag{3.55}$$

$\Delta P = P(t) - P_0$	Finite difference in pressure at time t and initial pressure
ΔV	Finite volume change
V_{CV}	Size of control volume

The bulk modulus relates the chamber pressure to difference in volume flow rate as:

$$P = P_0 + \frac{\beta}{V_{CV}}\int_{t_0}^{t} \Delta Q \; dt \tag{3.56}$$

Which corresponds to a C-element with compliance C defined as:

$$C = \frac{V_{CV}}{\beta} \tag{3.57}$$

Where the compliance is a function of the chamber volume, which is the original volume plus the change of control volume due to the moving boundaries as shown in equation 3.55.

$$\begin{aligned} V_A &= V_{A0} + \int_{t_0}^{t} Q_{AT} \; dt - \int_{t_0}^{t} Q_{Aspring} \; dt \\ V_B &= V_{B0} - \int_{t_0}^{t} Q_{AT} \; dt + \int_{t_0}^{t} Q_{Bspring} \; dt \end{aligned} \tag{3.58}$$

Spring-Piston

The energy flow rate in to the control volume due to deformation of the control volume is in (Çengel et al., 2010) defined as:

$$\dot{W}_{Piston} = \int_{CS1} P(\vec{V} \cdot \vec{n}) dS \tag{3.59}$$

Where:

P	Pressure in control volume
$\vec{V}$	Fluid velocity field
$CS1$	Surface of the control volume facing the spring
$\vec{n}$	Normal vector of the control surface

Since the normal component of the velocity at the spring surface is equal to the time derivative of the spring deflection $\vec{V} \cdot \vec{n} = \dot{w}$ along with the assumption that the pressure is constant throughout the chamber, can equation 3.59 be rewritten:

$$\dot{W}_{Piston} = \int_{CS1} P(\vec{V} \cdot \vec{n}) dS = P \int_{CS1} (\dot{w}) dS \tag{3.60}$$

For the hydraulic part of the model to comply with the spring model described in section 3.2, the spring is seen as n evenly distributed pistons as shown in figure 3.19. Each piston have an area $A_i = \frac{A_{Spring}}{n}$. Assuming this, equation 3.59 can be simplified:

$$\dot{W}_{Piston} = \int_{CS1} P(\vec{V} \cdot \vec{n}) dS \approx P \sum_{i=1}^{n} \dot{w}_i A_i \tag{3.61}$$

The volume change rate due to the n pistons deforming the control volume is equal to the sum of the contributions:

$$Q = \sum_{i=1}^{n} \dot{w}_i A_i \tag{3.62}$$

Equation 3.61 in combination with equation 3.62 corresponds to the power relations for a 0-junction as shown in figure 3.17.

The resulting force from the pressure acting on the spring is equal to the pressure times the area and the hydraulic part of the model can be related to the mechanical part using TF-element as shown in figure 3.17 with the area of the spring elements as modulus. The area of the spring elements is the total area of the spring facing the control volume divided by the number of elements:

$$F/A_i = P \tag{3.63}$$

Due to the large number of elements in the mechanical domain is the field bond graph representation used, so the demux block in 20-sim is used to sum the flows as shown in

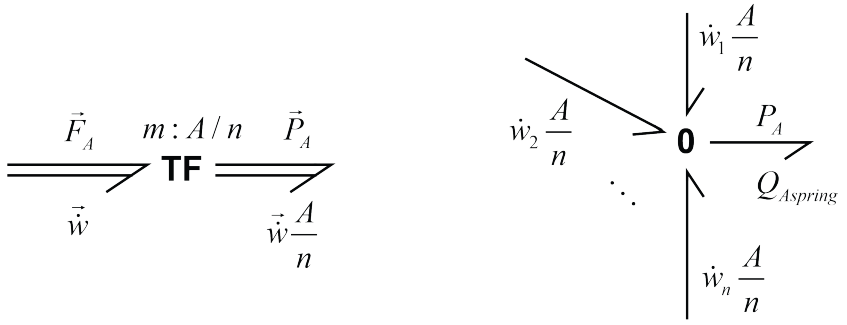

Figure 3.17: Piston work by spring

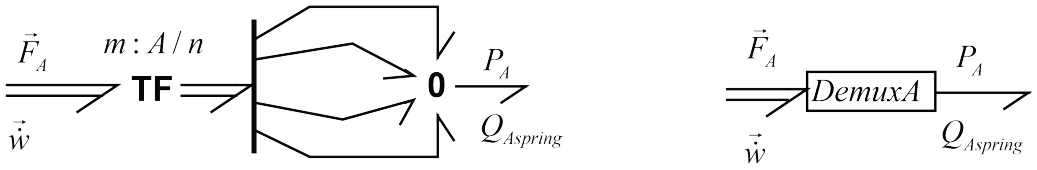

Figure 3.18: Demux A

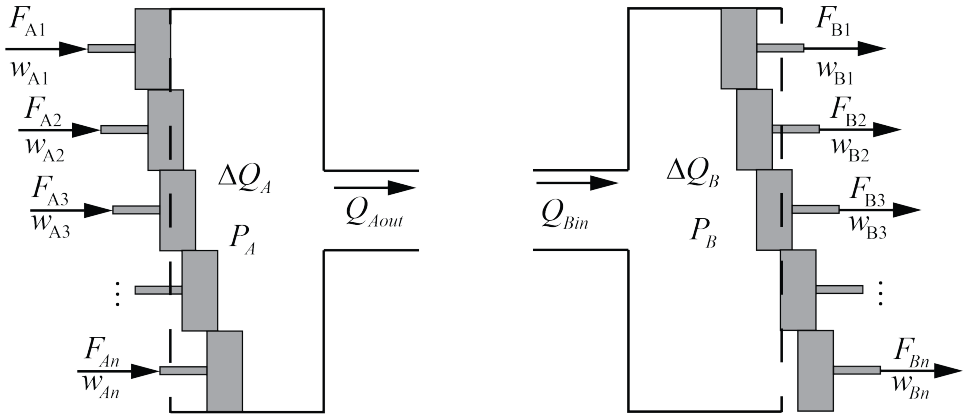

Figure 3.19: Demux B

figure 3.18. To make the model more comprehensible, the demux block and 0-junction are collected in the sub model DemuxA.

The same can be shown for oil chamber B, only the difference is that the positive power flow direction is defined as from the hydraulic domain to the mechanical domain as shown in figure 3.20. To make the model more comprehensible, the demux block and 0-junction are collected in the sub model DemuxB.

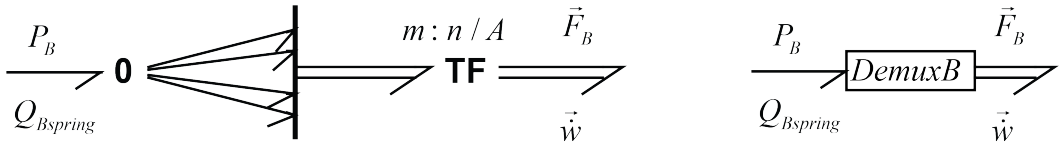

Figure 3.20: Spring piston simplification

Slit

Since the compressibility within the slit is neglected, the volume flow in and out of the slit is the same, and the slit volume flow is defined as:

$$Q_{Slit} = Q_{Aout} = Q_{Bout} \tag{3.64}$$

The pressure drop through the slit, which here is denoted ΔP_{Slit}, is the difference between the pressure in chamber A and chamber B. If equation 3.55 is multiplied by Q_{Slit}, the result is the energy flow rate relation for the slit which corresponds to a 1-junction.

$$\Delta P_{Slit} = P_A - P_B \tag{3.65}$$

The pressure drop through the slit assumed to follow the orifice equation as given in (Pedersen and Engja, 2008):

$$Q = sign\left(\Delta P\right) C_d A \sqrt{\frac{2}{\rho}\left|\Delta P\right|} \tag{3.66}$$

C_d	Coefficient of discharge
ρ	Fluid density
A_{Slit}	Slit area
ΔP	Pressure drop

This is a non linear relation between an effort and flow which corresponds to a R-element. The resulting bond graph relating the energy exchange through the slit is shown in figure 3.21

Using equation 3.66 in its original form will however cause problems with the numerical solver. As the pressure differences is close to zero will the volume flow gradient $\frac{\partial Q}{\partial \Delta P}$ go towards infinity. A small change in pressure will then cause an enormous change in fluid flow, which causes the system to vibrate. These vibrations are not physical. This problem is however avoided by using the relation shown in equation 3.67. The constants ,A,s and b are found through visual comparison of equation 3.67 and 3.66. Figure 3.22 shows the two functions compared. The approximation equation will only

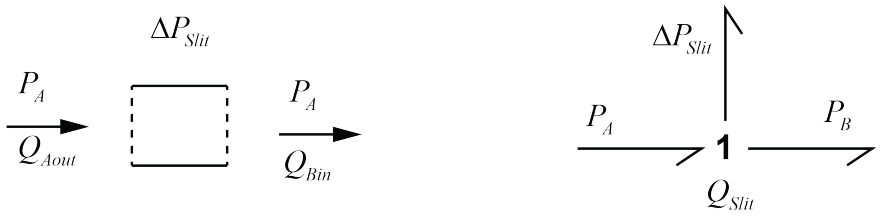

Figure 3.21: Volume flow and pressure drop through the slit

be valid for the pressure difference range used when fitting the curve. s Is the slope of the flow curve close to zero and b is the slope of the flow curve far from zero.

$$Q = C_D A_{Slit} \left(\frac{2}{\pi} A \arctan(s\Delta P) + b\Delta P \right) \tag{3.67}$$

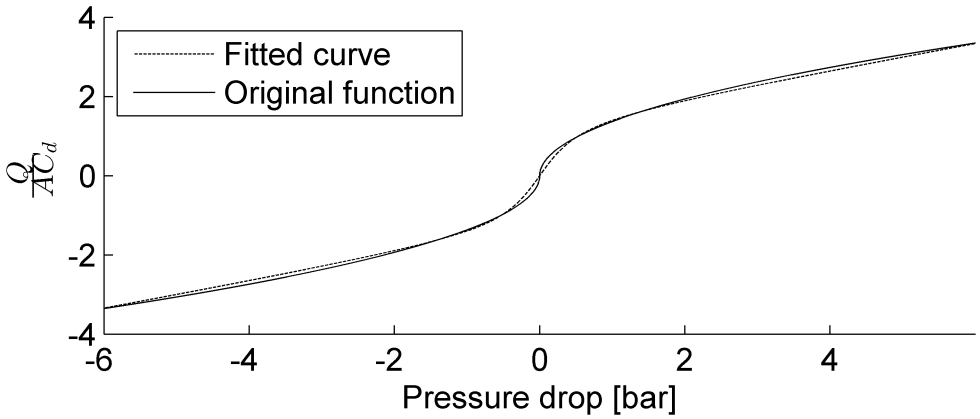

Figure 3.22: Comparison of the pressure flow relations in equation 3.67 and 3.66.

The final bond graph model relating the oil pressure to the spring deflection is shown in figure 3.23

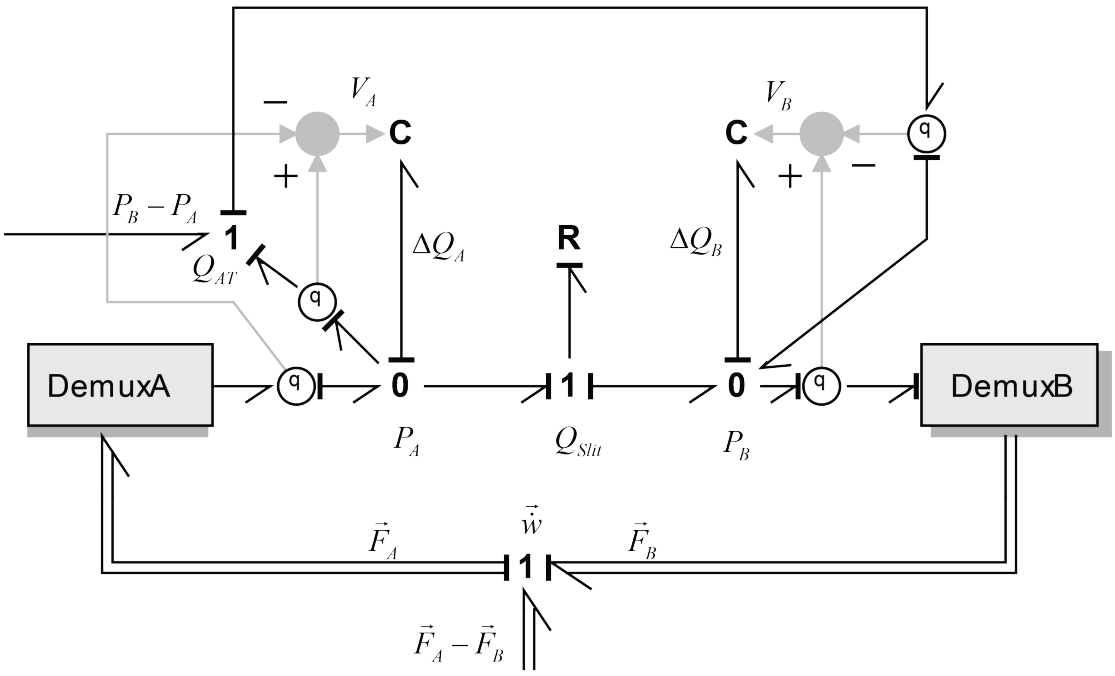

Figure 3.23: Hydraulic part of the flexicoupling model

3.4 Bumper

In (DNV, 2013a) it is required that the effect of any twist limiting devise is included in the model.

This is done in the Geislinger coupling when the spring hits the inner wall of the intermediate piece. This happens when the twist φ exeeds a maximum twist angle φ_{max}, as shown in figure 3.24

To incorporate this in the model a bumper is used. A bumper is in essence a C element with the stiffness of the system when the spring hits the wall. The C element is activated when the twist angle exceeds the maximum twist angle. In addition the bumper consist of an R element that dampen out the vibrations caused when the limiter is hit after a few Oscillations.

The damper is incorporated in to the model as shown in figure 3.26, between the 1-junction representing the nodal velocities. The stiffness of the wall is added to the stiffness of the flexible coupling.

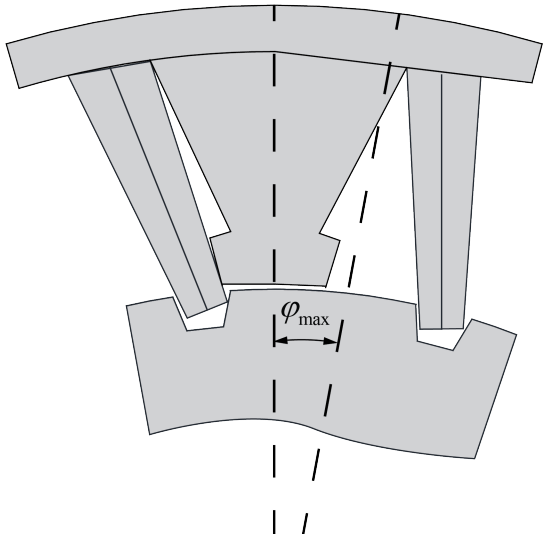

Figure 3.24: Detailed view of the flexible coupling as the maximum deflection is reached and the spring hits the twist limiter

When the absolute twist angle is below the twist limiting value K and B is zero and when the twist angle is above the twist limiting value K and B is set equal to K_{Bumper} and B_{Bumper}.

3.5 Combining the coupling model

To be able to combine the spring model with the hydraulic model and the global relations model, shown in figure 3.4, 3.13 and 3.23 respectively, the vector power bonds are expanded to comply with the vector power bonds going in to the spring. This is done using Se-elements with zero effort and mux/demux elements as shown in figure 3.25.

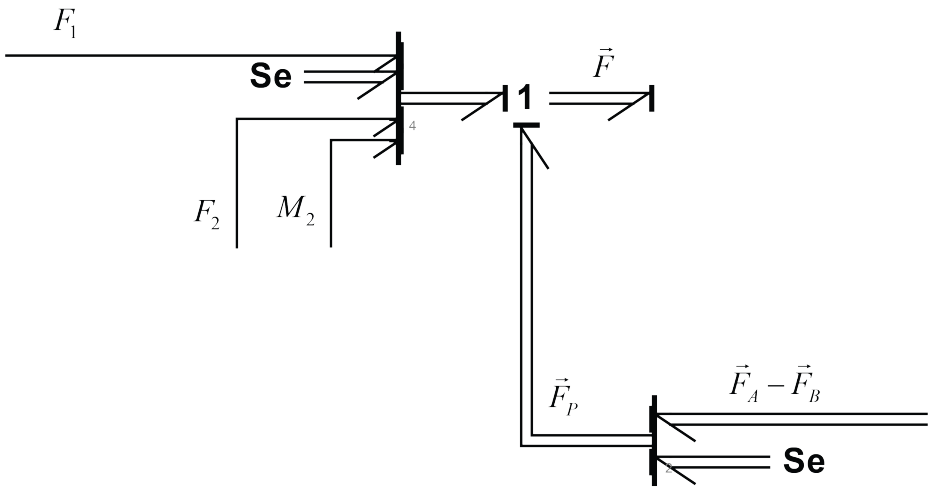

Figure 3.25: Expanding of the field bond graphs to comply with the spring using effort sources

The result is the power bond connected to the spring with the effort vector:

$$\vec{F} = \begin{bmatrix} F_1 \\ 0 \\ F_{P1} \\ 0 \\ F_{P2} \\ \vdots \\ F_2 \\ M_2 \end{bmatrix} \tag{3.68}$$

To avoid causality conflicts,in the 1-junctions representing the nodal velocities, is connection connection between the springs and the outer member not seen as completely rigid. I.e the outer member will deform due to the linear force from the spring. The spring connection will also inherit some damping, which is included using the R-element.

Causality conflicts makes the set of differential equations impossible to solve and must therefore be avoided.
Doing this, another state is included in the system, along with another natural frequency. The state in is self is not interesting, but this is a necessity to avoid causality conflicts.
The final Flexible coupling bond graph relating the external torques to each other is shown in figure 3.26.

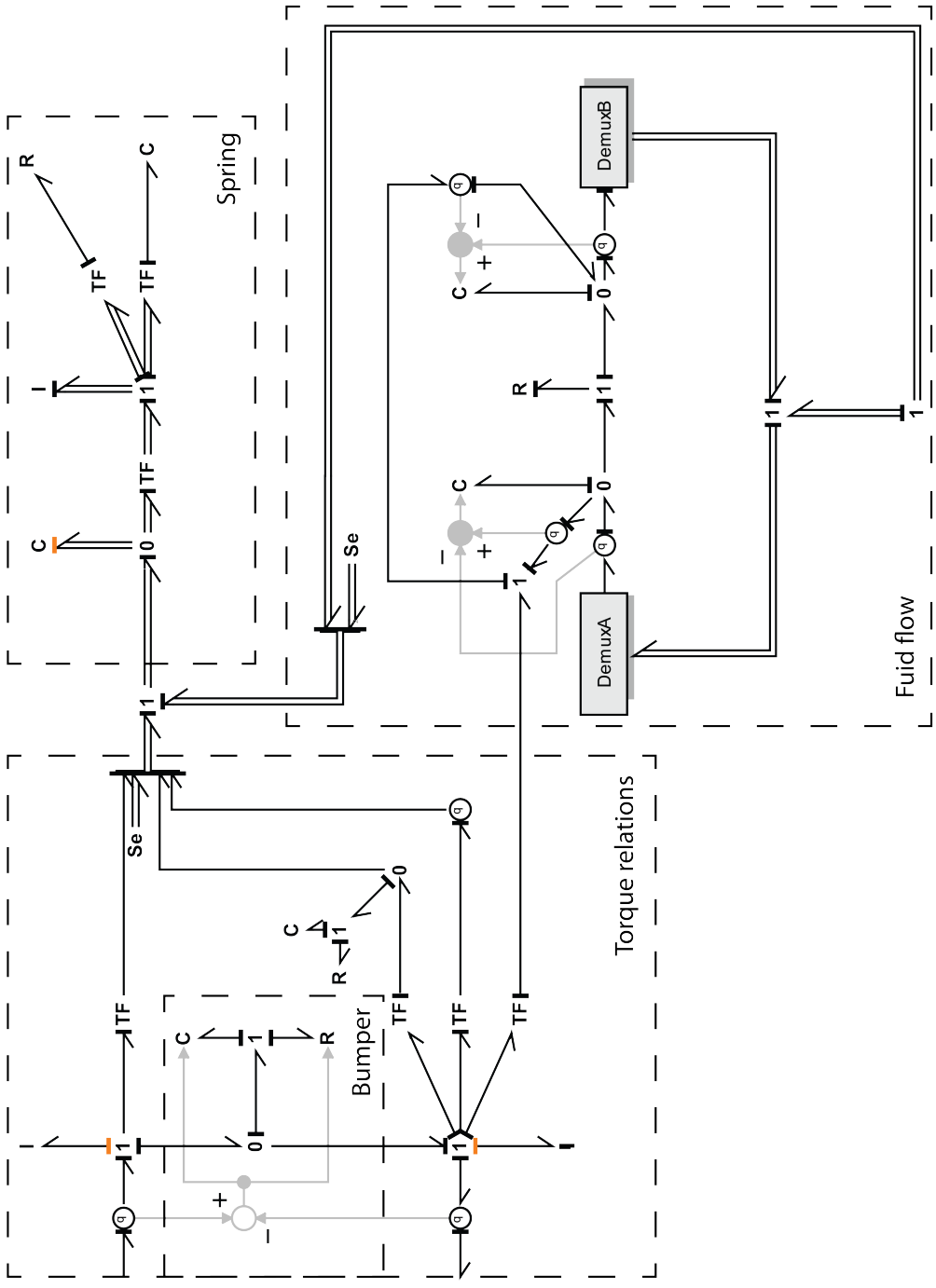

Figure 3.26: Flexible coupling bond graph relating the external torques to each other

Chapter 4
Model Verification

The flexible coupling model developed in chapter 3 is dependent on a number of parameters. Geometric parameters, material parameters and hydraulic parameters. Many of these parameters are dependent on each other and few of them are given by the flexible coupling manufacturer. The parameters which are not given by the manufacturer has to be approximated.

In this chapter is a selection of initial parameters chosen and verified.

4.1 Initial Parameters

The chosen coupling is the coupling with designation: B 110/10/45 UC/L A.1.

The designation stands for: Type of connection flanges / Outer diameter of centre part in centimetres. / Width of the spring pack in centimetres. / Stiffness series. / Reversible or non-reversible. / Left or right hand rotation.

The coupling is chosen based on the flexible coupling parameters presented in Polic et al. (2013), to get some reference. The limited information given by the manufacturer in the coupling catalogue Geislinger (2013), used in this model is listed in appendix A.1.

Since the detailed drawings of the coupling is not available at the time, are the measurements based on the drawings given in the Geislinger coupling catalogue Geislinger (2013). The drawings given here are given for illustrative purposes and are not correct for all the coupling models. This is however the only thing to base the dimensions on. So to get some idea of the dimensions, the drawings from the catalogue are scaled to fit the global dimensions presented in appendix A.1 using CAD software. The dimensions are then found by measuring the scaled drawing. The measured dimensions are presented in appendix A.2.
Using the measurements from the drawings and the parameters given by the man-

ufacturer are the rest of the geometric parameters found by using simple geometric relations. This is shown in appendix A.3.
The material of the spring is not given so the material properties of construction steel is used. These are listed in appendix A.4.
To find the modal damping ratio of the springs, experimental data would be needed. This is not available, however in (Karnopp et al., 2012a), it is argued that it is often enough to use modal damping ratios in the range of 0.01 to 0.1. The reference value is therefore set to 0.1.

4.1.1 Hydraulic parameters

In the coupling catlaogue given by (Geislinger, 2013) is it stated that the oil supply can come from the driving machinery, which means that the coupling uses the engine lubrication oil. The 2 stroke engine in the propulsion drive train, which the flexible coupling model is intended for, presented in (Polic et al., 2013), uses an engine oil presented in (Castrol, 2012). This is a mineral oil with a density of 890 kilo/m^3 at 15 °C and atmospheric pressure. The viscosity of the oil at 100 °C is 11.5 $mm^2\,s^{-1}$. In (Hodges, 1996) The typical bulk modulus of a mineral oil is given as 1.57 GPa.

In (Pedersen and Engja, 2008), the coefficient of discharge is said to lay within 0.6 to 0.65 for a valve opening if the orifice edges are sharp. The lower value is used for reference.

The curve fitting constants used in equation 3.67, were found using visual comparison between the fluid flow found from equation 3.67 and the approximation formula 3.66. The result is shown in figure 3.22

4.1.2 Twist limiter

The twist limiter stiffness is in reality a result of how the coupling deforms as the spring hits the twist limiter. To find a accurate value of this the coupling would have to be modelled using the finite element method and the exact dimensions of the coupling, which is not available as of now.

However to get some idea of the stiffness, the outer member is seen as rigid while the twist limiter is seen as a bar subjected to longitudinal deformation. The stiffness of the twist limiter is then 7e10 [$N\,m\,rad^{-1}$]. The calculations are shown in section A.6. This value is however too high as both the spring hitting the twist limiter and the intermediate piece has stiffness. To get some reference, the bumper stiffness is set to

one third of the maximum stiffness $K_{Bump} = 2.35e10$.

The bumper damping coefficient b_{bump}, is found by visual interpretation of the bumper deformation. The value is set such that the bumper deflection oscillations dies out after a number of oscillations, when subjected to a sudden load. As a reference b_{Bump} is set to the value of the bumper stiffness times 1e-5.

The stiffness and damping coefficient of the compliance element fixing the radial spring to the outer member is comparable to the stiffness and damping coefficient of the twist limiter since both depend on the stiffness of the outer member, and is therefore given the same value. In other words, the uncertainty of both is comparable.

4.1.3 Fixing the coupling

To investigate how the coupling acts as it is subjected to harmonic loads, the coupling is fixed at the outer member which is the node closes to the propeller. This is done using a Sf element with zero velocity. To avoid causality conflicts, a C-element is added between the coupling and the fixing point. This is comparable to connecting a short piece of propeller shaft to the coupling and fixing one end. This adds another another state to the coupling system, along with another natural frequency. The value of this compliance is not important as long as it is high enough and does not affect the system response at the operating frequencies experienced by the coupling.

4.1.4 Static stiffness

The natural place to start the parameter study the static stiffness of the coupling, as it depends on the fewest variables. The static stiffness is given by the manufacturer, and for the chosen coupling the values are shown in appendix A.1.

The static stiffness is the rotational stiffness of the coupling as the coupling is twisted at low frequencies. The static stiffness depends on the geometry of the spring and the inner and outer member. More specific the cross sectional area of the spring, the radii of the inner and outer member and the number of spring/oil-cells.

In (Geislinger, 2013), the manufacturer states that the rotational stiffness of the coupling is linear up to values 1.4 times the nominal torque. This means that the tapered springs behaviour is close to a springs with constant cross sectional area below 1.4 times the nominal torque.

Figure 4.1 shows a torque versus twist plot of the damper as it is clamped in one end and excited by a harmonic force with a low frequency ($\omega = 1[\mathrm{rad\,s^{-1}}]$) and a amplitude

equal to 10 % of the nominal torque. The force is completely reversed.

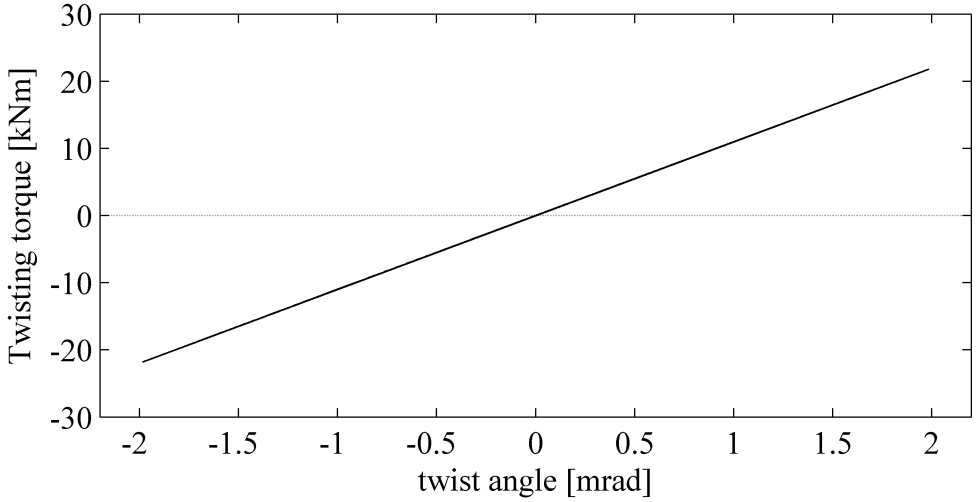

Figure 4.1: Hysteresis plot of the damper as it is clamped in one end and excited by a completely reversed harmonic force with $\omega = 0.1[\mathrm{rad\,s^{-1}}]$ and a amplitude equal to 10 % of the nominal torque.

The stiffness is clearly constant in this region.
From figure 4.1, using equation 2.10 the static stiffness is found to be 10.98 $[\mathrm{MN\,m\,rad^{-1}}]$, which is 233% of the value given by the manufacturer.

4.2 Improving the Static Stiffness

The stiffness value found in the previous section is too high. This means that one or more of the geometric parameters chosen is wrong. Next the effect of changing the spring cross sectional area and the spring length is investigated.
By changing the height of the spring profile, the static stiffness changes as shown in figure 4.2.

Changing the spring length can be done in two ways, either changing the radius of the inner member, or the radius of the outer member. Figure 4.3 and 4.4 shows how the stiffness of the coupling changes with changing r1 and r2.

There is a infinite number of combinations within the boundary conditions given by the manufacturer that produce the same static stiffness, so finding the correct dimensions based on the static stiffness is impossible. However by changing the profile height

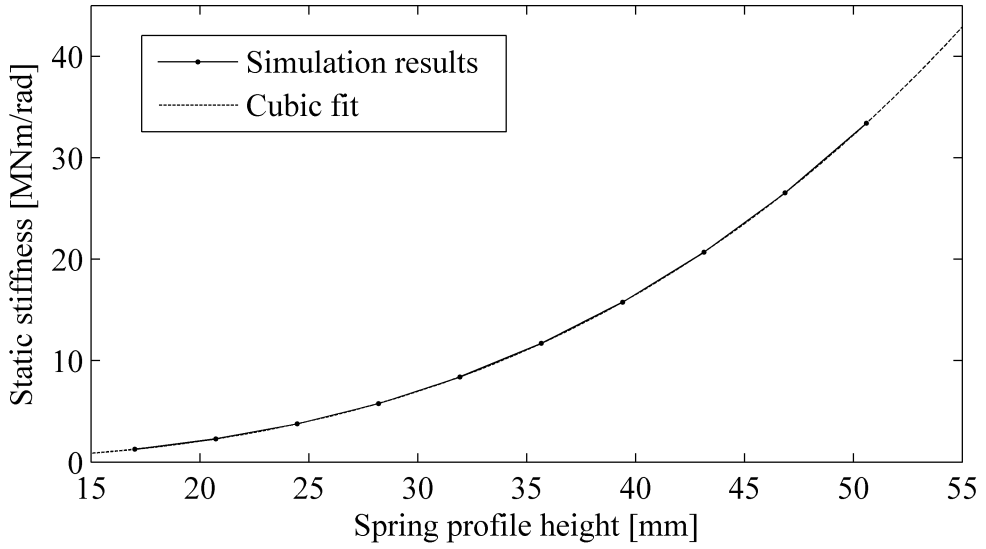

Figure 4.2: Static rotational stiffness of the coupling at different spring profile heights

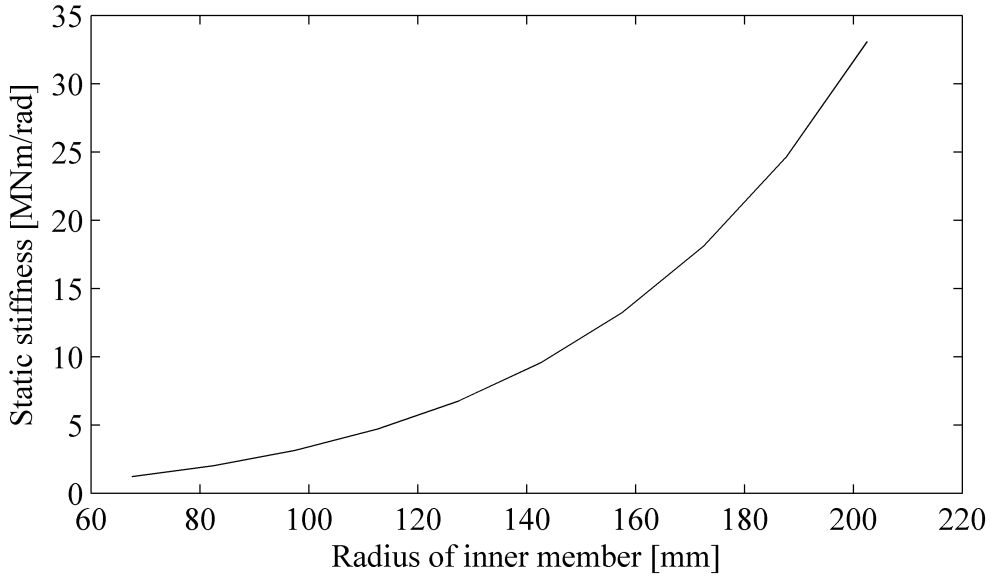

Figure 4.3: Static rotational stiffness of the coupling at different radii of the inner member

to 26.3 mm, the coupling model exert the same stiffness as the data given by the manufacturer and this will be used as a basis from now on.

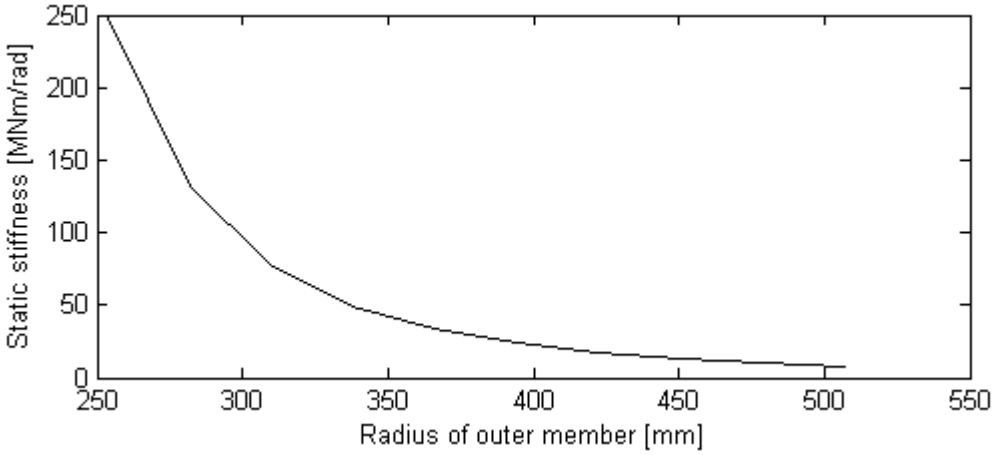

Figure 4.4: Static rotational stiffness of the coupling at different radii of the outer member

4.2.1 Spring flexible modes

Having established the dimensions of the spring, the natural frequencies of the spring can be found using equation 3.12 from section 3.2. The first natural frequency of the spring is 6148 [rad s^{-1}]. This is 8.9 times the characteristic coupling frequency of the coupling and more five hundred times the rated RPM of the engine. It is therefore safe to assume that the spring will not vibrate at any of the flexible modes. In (Karnopp et al., 2012b) it is recommended to keep flexible modes with natural frequencies that are from two to five times the frequencies experienced by the system.

The spring model is therefore reduced to the bond graph shown in figure 4.5. Where all the flexible modes are included in the residual matrix. The transfer matrix contain only contributions from the solid body motion modes as shown in equation 4.1, while the modal mass matrix contains the mass and rotational inertia of the spring, m_spring and J_{spring}.

$$[r_1] = \begin{bmatrix} Y_1(x_1) & \frac{\partial}{\partial x}Y_{00}(x_1) & Y_{00}(x_2) & \frac{\partial}{\partial x}Y_{00}(x_2) & \cdots & Y_{00}(x_i) & \frac{\partial}{\partial x}Y_{00}(x_i) \\ Y_0(x_1) & \frac{\partial}{\partial x}Y_0(x_1) & Y_0(x_2) & \frac{\partial}{\partial x}Y_0(x_2) & \cdots & Y_0(x_i) & \frac{\partial}{\partial x}Y_0(x_i) \end{bmatrix} \tag{4.1}$$

$$I = \begin{bmatrix} m_{Spring} & 0 \\ 0 & J_{Spring} \end{bmatrix} \tag{4.2}$$

Where the solid body motion modes are:

$$\begin{aligned} Y_{00} &= 1 \\ Y_0 &= x - \tfrac{L}{2} \end{aligned} \tag{4.3}$$

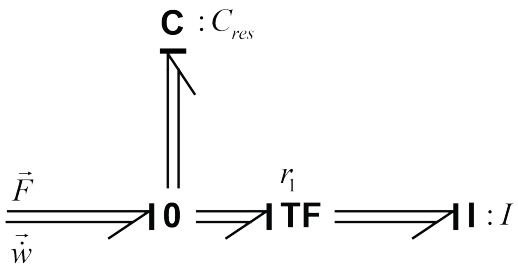

Figure 4.5: Bond graph model of the radial springs, including no flexible modes

And x, is position along the spring and x_i is the output positions of the spring as explained in section 3.2.

4.3 Dynamic Stiffness and Damping

Having established reasonable reference geometric parameters, the frequency response of the flexible coupling can be investigated. The best means of comparing the flexible coupling model developed in this master thesis with the original Geislinger flexible coupling, is by comparing the dynamic stiffness and damping factor. These are as shown in section 2.3.1, presented for a frequency range up to the characteristic coupling frequency in (Geislinger, 2013).

The damping factor and stiffness of the coupling at varying frequencies is found using the method described in section 2.2. The hysteresis loop is found at different frequenciesby clamping the coupling at the node facing the propeller and subjecting the node facing the engine to a harmonic load. The load 10% of the nominal torque of the flexible coupling. For the zero flow boundary to be possible to impose on the coupling, a stiff compliance element is included between the zero flow boundary and the coupling. This is comparable to connecting the coupling to a fixed base using a short shaft element. The inertia of the inner and outer member is not included in the simulations, as including them would would shift the hysteresis plot and the coupling stiffness and damping would not be correct.

The displacements found from the simulations are not completely stable, in that the displacement varies somewhat between the different loading and unloading cycles. This is due to integration errors by the numeric solver in 20-sim. Since the results vary is the data presented using the mean value and the coefficient of variance.

The hysteresis loop of the coupling found using the parameters presented in appendix A.1 and the spring profile height found in section 4.2, is shown in figure 4.6 and 4.7. Figure 4.8 and 4.9 shows how the coupling stiffness and non dimensional damping factor found from the simulations plotted against the values given by the coupling manufacturer.

4.3.1 Results

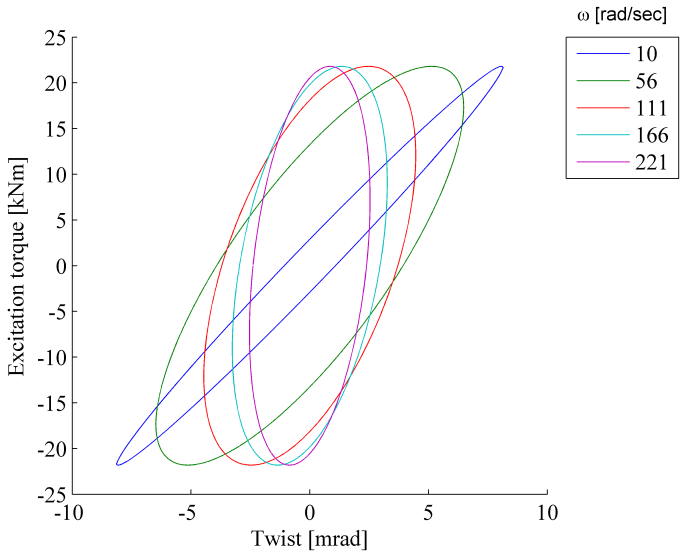

Figure 4.6: Coupling twist through a loading cycle plotted agaisnt excitation torque at different excitation frequencies

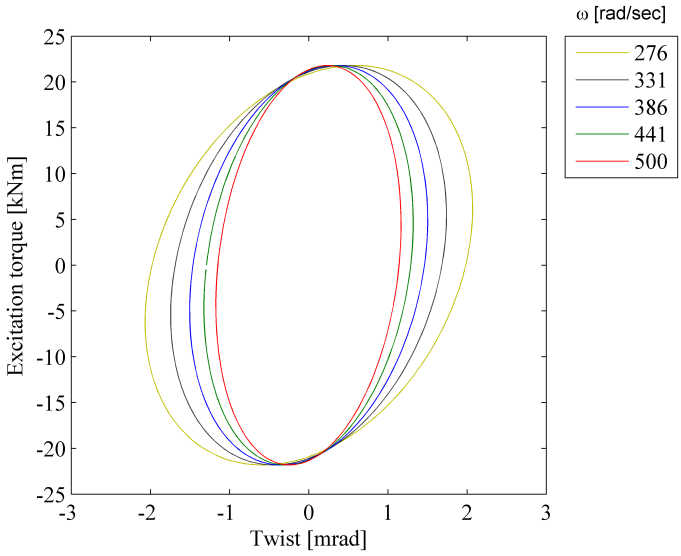

Figure 4.7: Coupling twist through a loading cycle plotted agaisnt excitation torque at different excitation frequencies

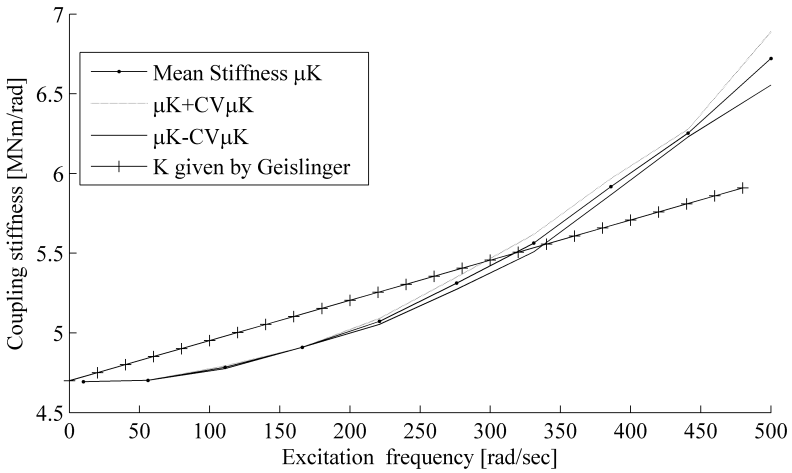

Figure 4.8: Coupling stiffness at different excitation frequencies found by simulation plotted against the stiffness given the coupling stiffness given by the manufacturer

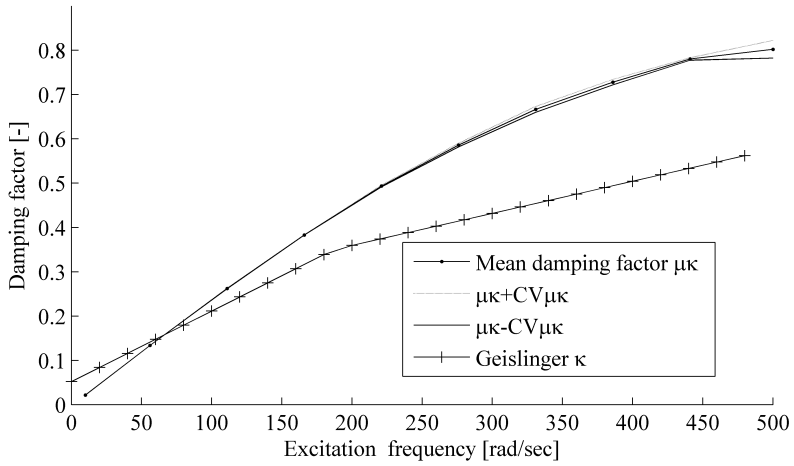

Figure 4.9: Non dimensional damping factor at different excitation frequencies found by simulation plotted against the stiffness given the coupling stiffness given by the manufacturer

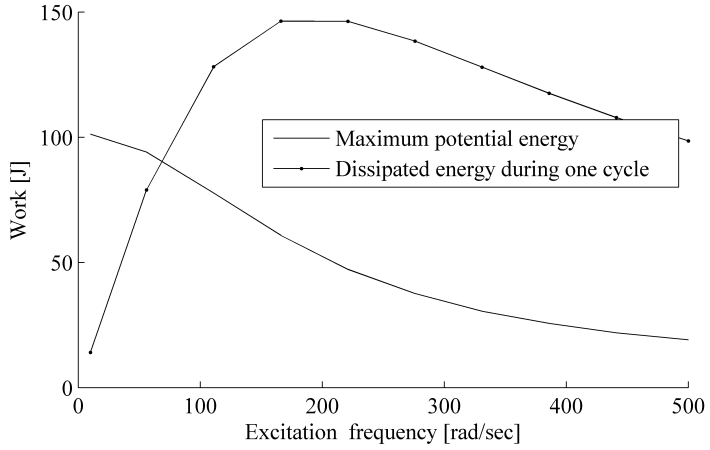

Figure 4.10: Maximum elastic potential energy and amount of energy dissipated by the coupling through one loading cycle at different frequencies

Figure 4.11 and 4.12 shows how the volume flow through the slit and pressure difference between chamber a changes with changing excitation frequency

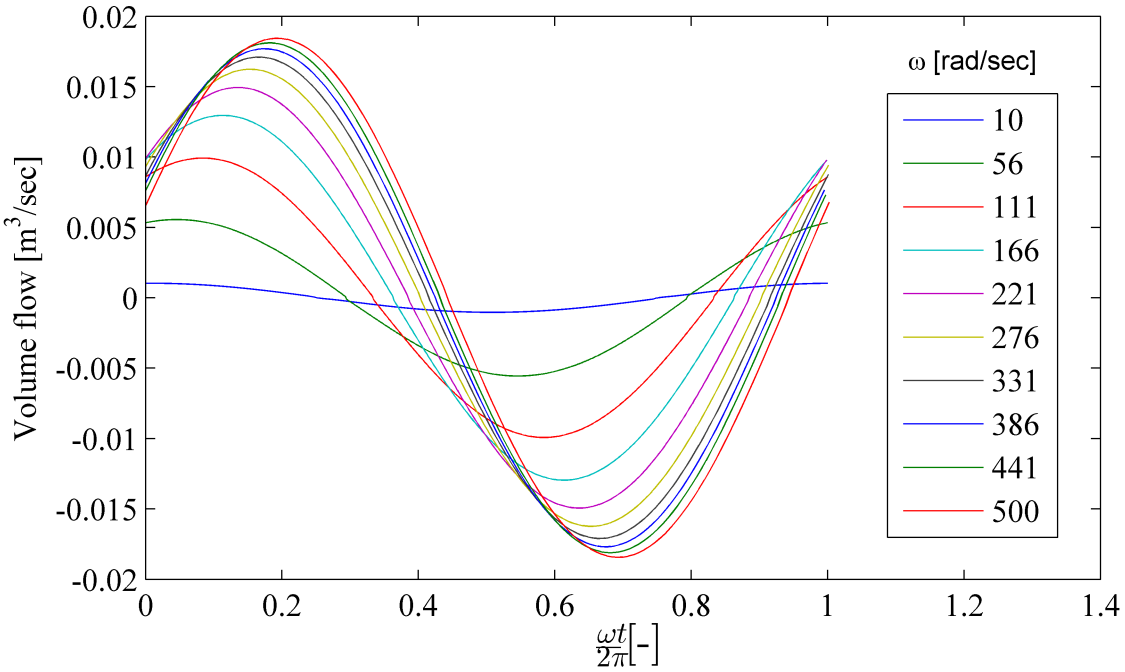

Figure 4.11: Volume flow through slit at different excitation frequencies

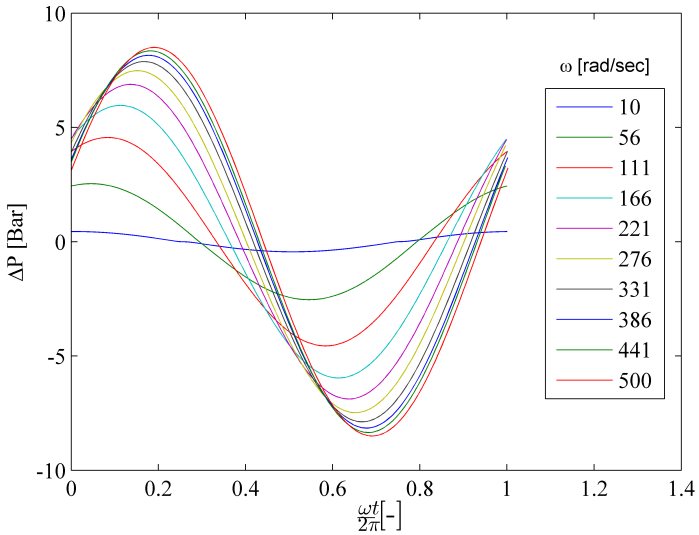

Figure 4.12: Pressure difference between oil chambers at different excitation frequencies

Figure 4.13 and 4.14 shows how the chamber volume of chamber A and chamber b changes with changing excitation frequency throughout a loading cycle.

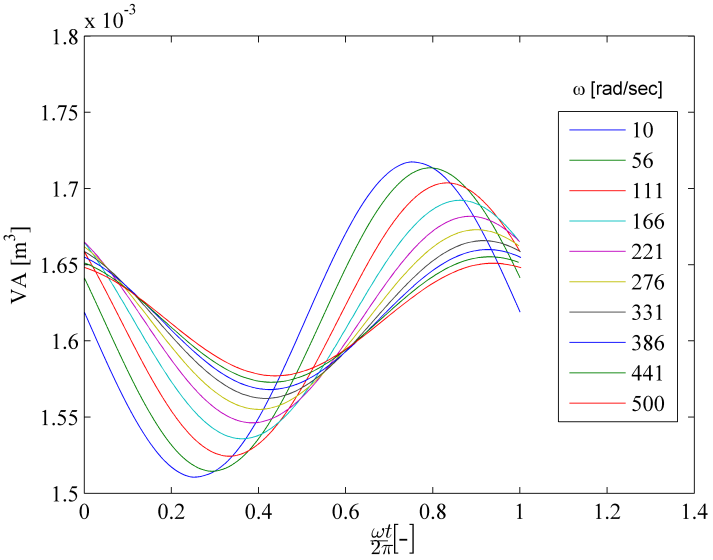

Figure 4.13: Chamber volume of chamber A throghout a loading cycle at different excitation frequencies

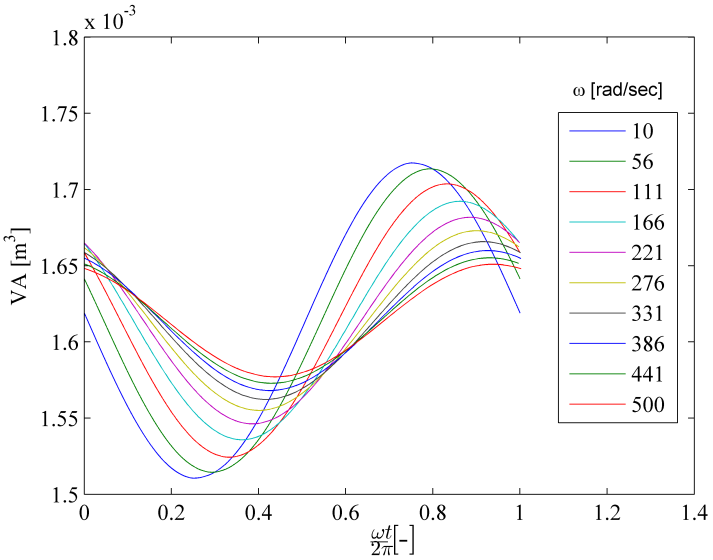

Figure 4.14: Chamber volume of chamber B throghout a loading cycle at different excitation frequencies

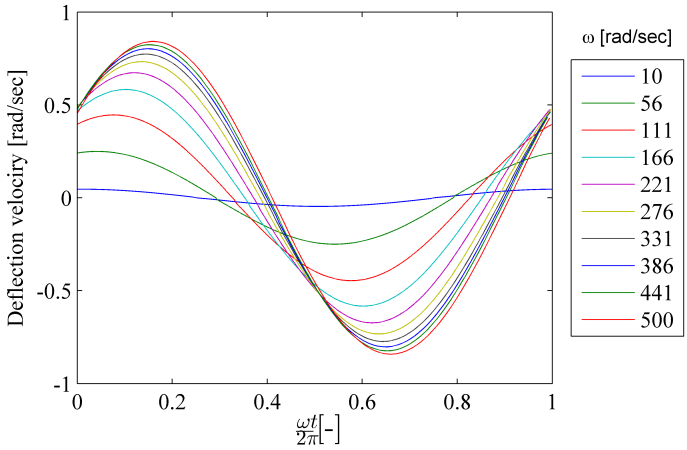

Figure 4.15: Rate of coupling deflection, $\dot{\varphi}$, at different excitation frequencies

4.3.2 Discussion

The gradient of the hysteresis loop increases with frequency within the frequency range evaluated, as shown in figure 4.6 and 4.7. The difference between the minimum and maximum coupling twist decreases while the difference between the torque at these points increases. This causes the stiffness to increase as shown in figure 4.8.

Another thing that is apparent from the hysteresis plot (figure 4.6 and 4.7) is that the maximum deflection occurs later and later relative to the maximum torque. This is since the damping torque is phase shifted 90° relative to the elastic torque. As the size of the damping torque increase, so will the phase shift between the deflection and damping torque.

The stiffness increases at higher frequencies since to the change in oil chamber volume has to happen faster at higher frequencies. Due to the volume flow-pressure relation in equation 3.67, is a higher pressure required to increase the volume flow. Since less oil escapes than the volume changes will the oil have to compress. The consequence is that, as the excitation frequency increases so does the amount of oil that have to be deformed.

The extreme cases would be; no flow restrictions and completely stopping the flow between the chambers. If there is no flow restriction the stiffness of the coupling would be the same as the static stiffness, and if the flow was completely stopped would the coupling inherit both the stiffness of the spring and the oil. Figure 4.8 shows that the coupling stiffness at low frequencies is close to the static stiffness.

From figure 4.8 it can be seen that the stiffness gradient is a function of excitation fre-

quency, and within the frequency range evaluated will decrease at higher frequencies. Since the stiffness increases at higher deflection velocities, and because the amplitude of the torque excitation is kept constant, the coupling deformation will become smaller. As a consequence, the deformation rate does not increase linearly with excitation frequency. Figure 4.15 shows how the change in coupling deflection rate reduces at large velocities. Since the change in the coupling deflection rate is lower at high frequencies, the change in oil flow velocity will follow the same trend. This causes the decrease in the stiffness gradient.

Figure 4.10 shows how the maximum potential energy decreases at higher frequencies. The reason for this is the increasing stiffness, which causes a smaller coupling twist at higher frequencies.

The dissipated energy is as shown in equation 2.4, the excitation torque times the coupling deflection rate, integrated over a period. The coupling deflection rate change decreases as mentioned at higher excitation frequencies. This in addition to the fact that the excitation period changes inversely with the excitation frequency, causes the energy dissipated during one excitation cycle to increases until it reaches a maximum value, then decrease. This can be seen from figure 4.10. This can also be observed in the hysteresis curves shown in figure **??** and **??**, since the dissipated work is the area enclosed by the curve as explained in section 2.2.

The damping factor is as stated in section 2.2 defined as the relationship between the dissipated energy and the maximum elastic energy during one loading cycle times 2π. As shown in figure 4.10 is the gradient of the maximum potential energy during a cycle times 2π , lower than the gradient of the dissipated energy. As a consequence increases the damping factor as shown in figure 4.9.

4.4 Improving the Dynamic Stiffness and Damping

The stiffness and damping coefficient found in the previous section are not equal to the values given by the manufacturer. Next is the effect of changing the coefficient of discharge investigated, to see if it is possible to improve the dynamic stiffness and damping characteristics of the flexible coupling model.

Figure 4.17, shows the effect of changing the coefficient of discharge on the coupling stiffness, while figure 4.17 and 4.18 shows the effect on the coupling damping and dissipated energy respectively. The values checked range from 0.5 to 0.7.

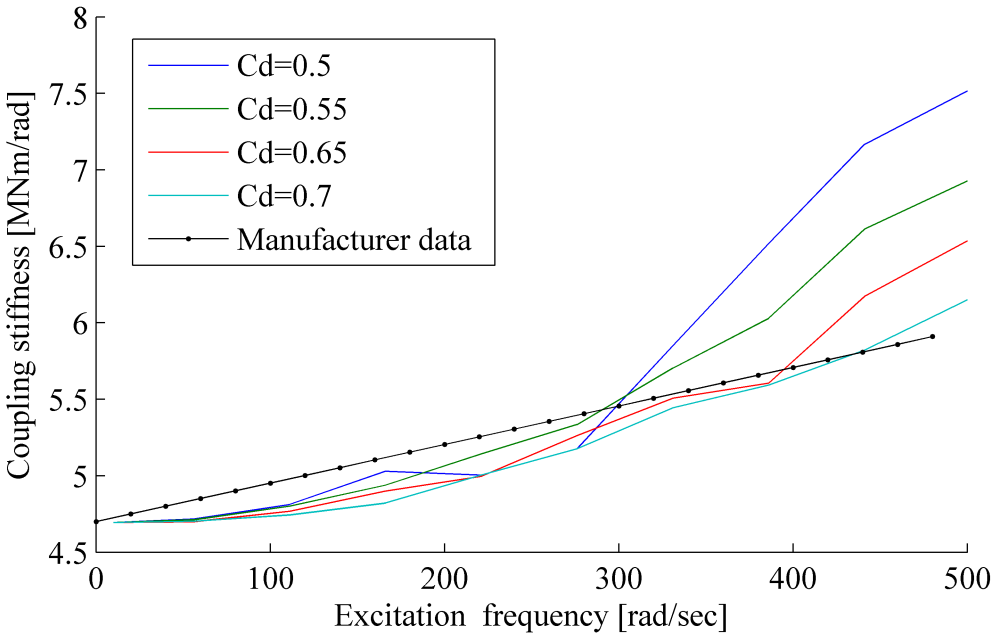

Figure 4.16: Coupling stiffness at different excitation frequencies and different discharge coefficients, found by simulation. Plotted against the stiffness given the coupling stiffness given by the manufacturer

4.4.1 Effect of changing the coefficient of discharge

The results show that when using higher Cd values does the coupling stiffness gradient decrease. The reason for this is that a lower pressure difference is required to obtain a oil flow velocity. This means that the amount of oil that is compressed is smaller at the same excitation frequency, and the stiffness is lower.

Using a discharge coefficient of 0.7 give similar coupling stiffness as the manufacturer gives. This does however not mean that this is the correct value. The coefficient of discharge times the slit area is from Pedersen and Engja (2008) given as:

$$C_D A = \frac{Q}{\sqrt{\frac{2}{\rho}\Delta P}} \tag{4.4}$$

Where

C_D	Coefficient of discharge
ΔP	Pressure difference over the slit
Q	Volume flow
rho	Fluid density

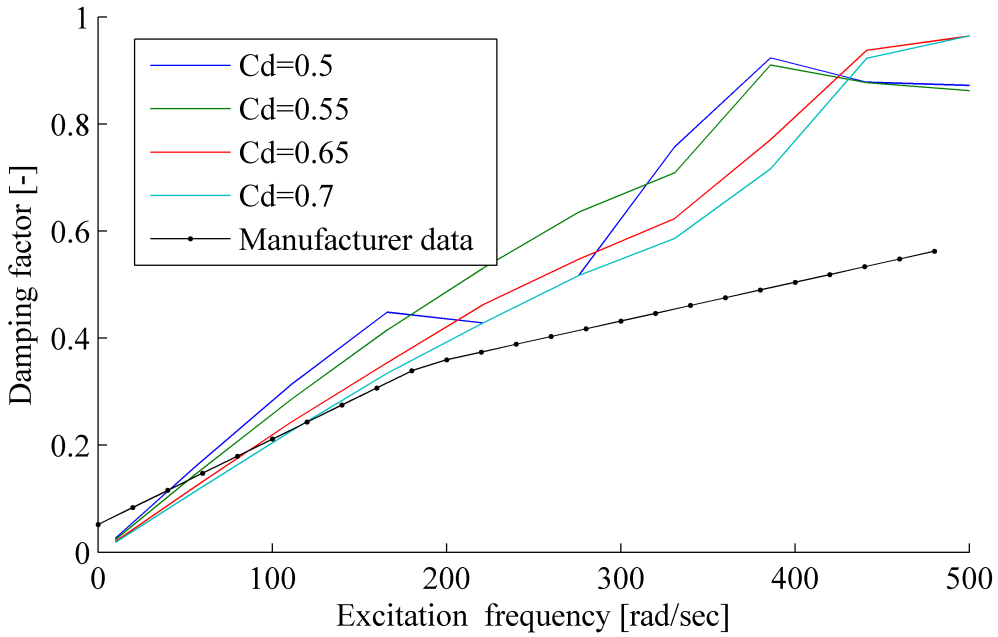

Figure 4.17: Non dimensional damping factor at different excitation frequencies and different discharge coefficients, found by simulation. Plotted against the stiffness given the coupling stiffness given by the manufacturer

An infinite number of C_D and A values would produce the same pressure-flow relationship. The slit area is given explicitly by the manufacturer for a single oil chamber, unfortunately is the number of oil chambers given directly and are found using the approximation described in section 4.

However, both the stiffness and damping factor using the discharge coefficient of 0.7 are closer to the data given by the manufacturer than the other values as shown in figure 4.17. The reason for the damping factor decreasing at higher discharge coefficients is that the amount of energy required to push a amount of fluid through is lower for a higher discharge coefficient causing.

Since a discharge coefficient of 0.7 gives the closes results is this used next.

4.5 Discussion

The model developed in this master thesis, called coupling-M, has several limitations. First of all does coupling-M not include the tapered radial springs as the Geislinger model has. As mentioned in (Geislinger, 2013), does the spring stiffness behave lin-

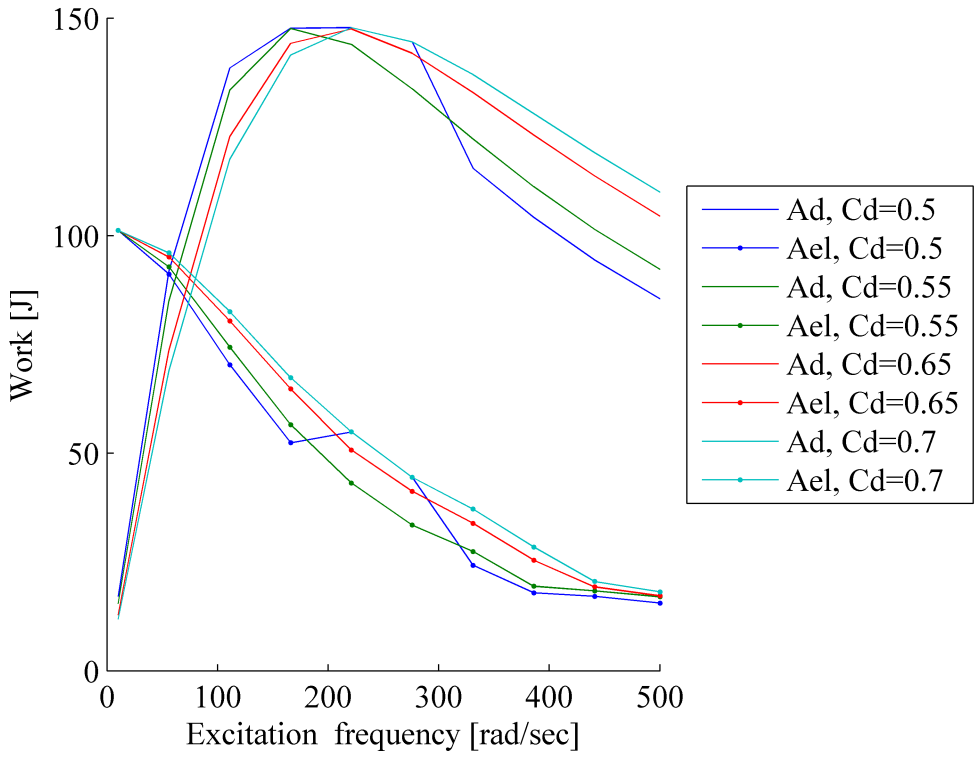

Figure 4.18: Maximum elastic potential energy, Ad, and amount of energy dissipated by the coupling through one loading cycle, Ael, at different frequencies and different discharge coefficients.

early up to 1.4 times the nominal torque. Up to this limit it can be assumed that coupling-M spring stiffness is a good representation of the Geislinger coupling spring stiffness. However at higher excitation torque values, as the ones experienced during ice-propeller interactions, the coupling-M stiffness is not a good representation of the Geislinger coupling spring stiffness.

Coupling-M does not include fluid inertance. This might be reasonable to assume as the velocities at which the fluid travels is lower than the speed of sound in the oil, but this has to be verified by including it in the model.

Another thing is that the volume change due to the spring deflection is a approximation, as explained in 3.3. Since the volume change is one of the things that affect both the damping and stiffness, might this be of grate importance.

The effect of air in the oil on the compressibility is not included. The effect of including the air compressibility is grates at low pressures. Low pressures might occur in the

oil chamber where the volume increases, and depends on the initial pressure in the chambers.

Even though the dynamic stiffness and damping factor of coupling-M are comparable to the data given by the manufacturer, will there be an infinite amount of parameter combinations that produce the same characteristics.

While some of the geometric parameters are given explicitly by the manufacturer, Is most of the geometric parameters found as described in section 4 and there is uncertainties connected to the them.

Last but not least is the coefficient of discharge assumed to be constant. This might be reasonable but needs to be determined through CFD calculations.

Chapter 5
Case Study

5.1 Drive train model

The coupling model developed in section is using the parameters found in section 4, included in a propulsion drive train model as shown in figure 5.1. The model including this coupling is referred to as coupling-M.
In (Polic et al., 2013), the author explains how the model is built up from a engine, propeller shaft and propeller:

The engine is a effort source controlled by a PI regulator setting the torque based on a RPM input. Included in the engine model is also the crank shaft inertia and mechanical loss using an I and R element respectively. One change is made however. The engine torque of the original model is constant. This is not the case for a real propulsion drive train, as the gas forces acting on the piston and the pistons movement will cause torsional vibrations in addition to the mean torque. As a reference is a harmonic load of 1% of the nominal torque added to the torque constant engine torque. The frequency of this harmonic component correspond the 7th engine order. Without this, the coupling developed in this master thesis would not have had the correct damping and stiffness characteristic.

Next, the propeller shaft is modelled using the finite mode superposition method described in section 3.2 only for the torsional domain. In addition to the solid body mode are three flexible modes included.

While the propeller model consists of the propeller inertia and the hydraulic resistance working on the propeller described by the propeller law. In addition to the inertia and hydraulic resistance does the R-element include the ice-propeller interaction law explained in section 2.5.

In addition to this the original model uses a flexible coupling with linear damping

coefficient and stiffness. The stiffness value used is the static stiffness of the coupling, while the damping coefficient corresponding to a deflection rate of 43 [rad s^{-1}]. The flexible coupling parameters correspond to the same coupling as the coupling model developed in this master thesis was developed from (Table A.1).

The original bond graph model including the coupling as a linear stiffness and damping element is shown in figure 5.2. The model is used for comparing the performance of couplin-M and is referred to as coupling-ref.

5.1.1 Difference between the flexible coupling model modules

The main differences between coupling-M and coupling-ref listed below: **Coupling-ref:**

- The flexible coupling stiffness is included as a C-element with constant stiffness with respect to coupling deflection magnitude and coupling deflection frequency and velocity.
- The torque acting on both the engine and propeller side of the coupling is always equal.
- The flexible coupling includes no twist limiting device.

Coupling-M:

- The radially aligned springs are included using constant cross sectional area, making the spring stiffness linear with respect to deflection.
- The coupling stiffness changes with coupling deflection velocities. This is due to the oil compressibility and fluid flow between the chambers as explained in section 4.3.2
- The damping effect of the oil flow between the chamber is included, causing the damping coefficient to change as a function of deflection velocity as explained in section 4.3.2.
- The model includes a twist limiter, which causes significant change of coupling stiffness as the maximum twist angle is reached and the twist limiter is engaged.

5.1.2 Loading conditions

The behaviour of coupling-M is compared to coupling-ref. This is done by subjecting the propulsion drive train to the Ice propeller interaction torque designated "Torque

excitation Case 1" in (DNV, 2013b) for the ice class designated ICE 1A. The torque profile is shown in figure 5.3. The engine torque is applied in two steps. After 5.5 second reaches the engine full speed. At this point is the ice propeller load introduced.

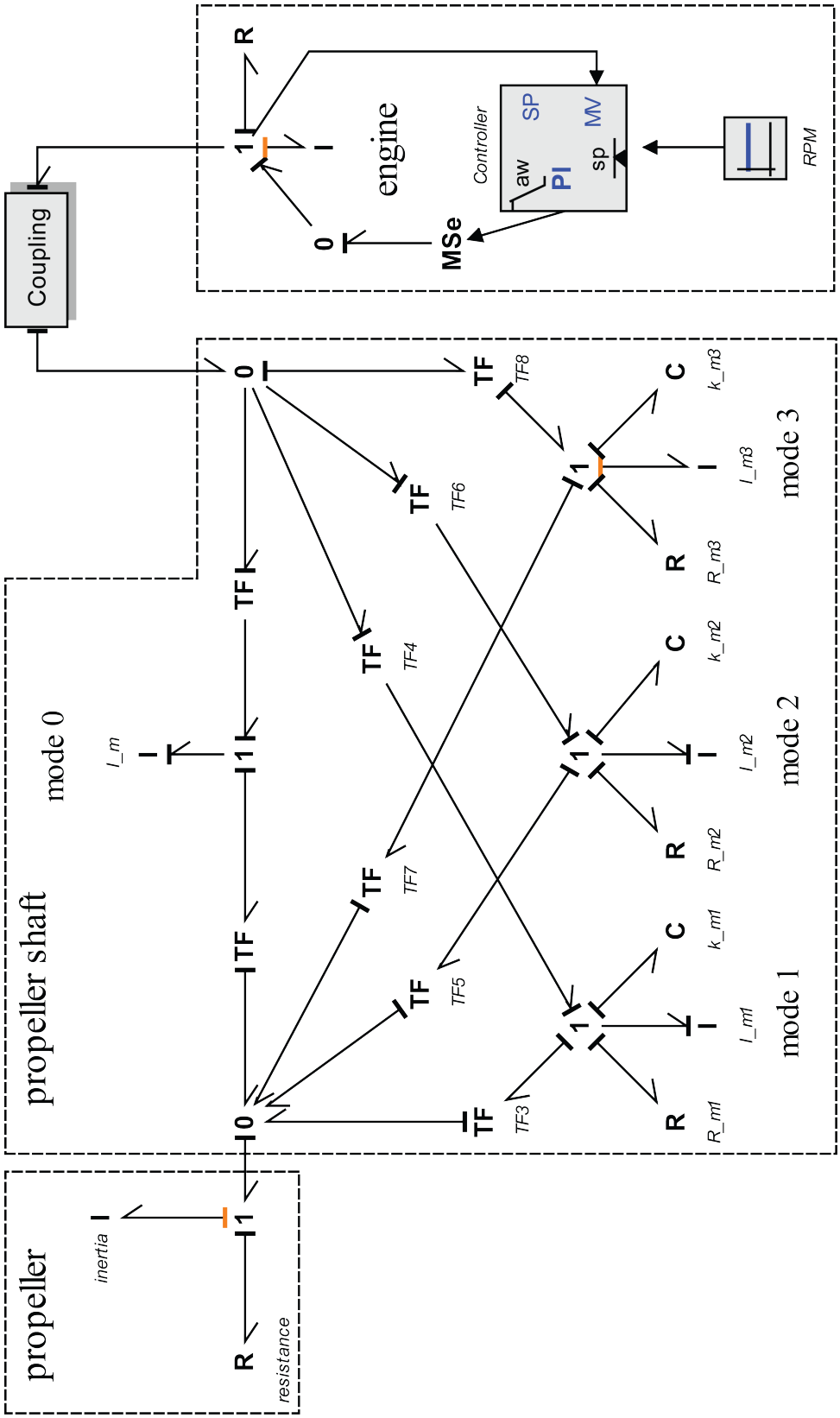

Figure 5.1: Figure showing the bond graph model of a propulsion drive train presented in (Polic et al., 2013) including coupling-M

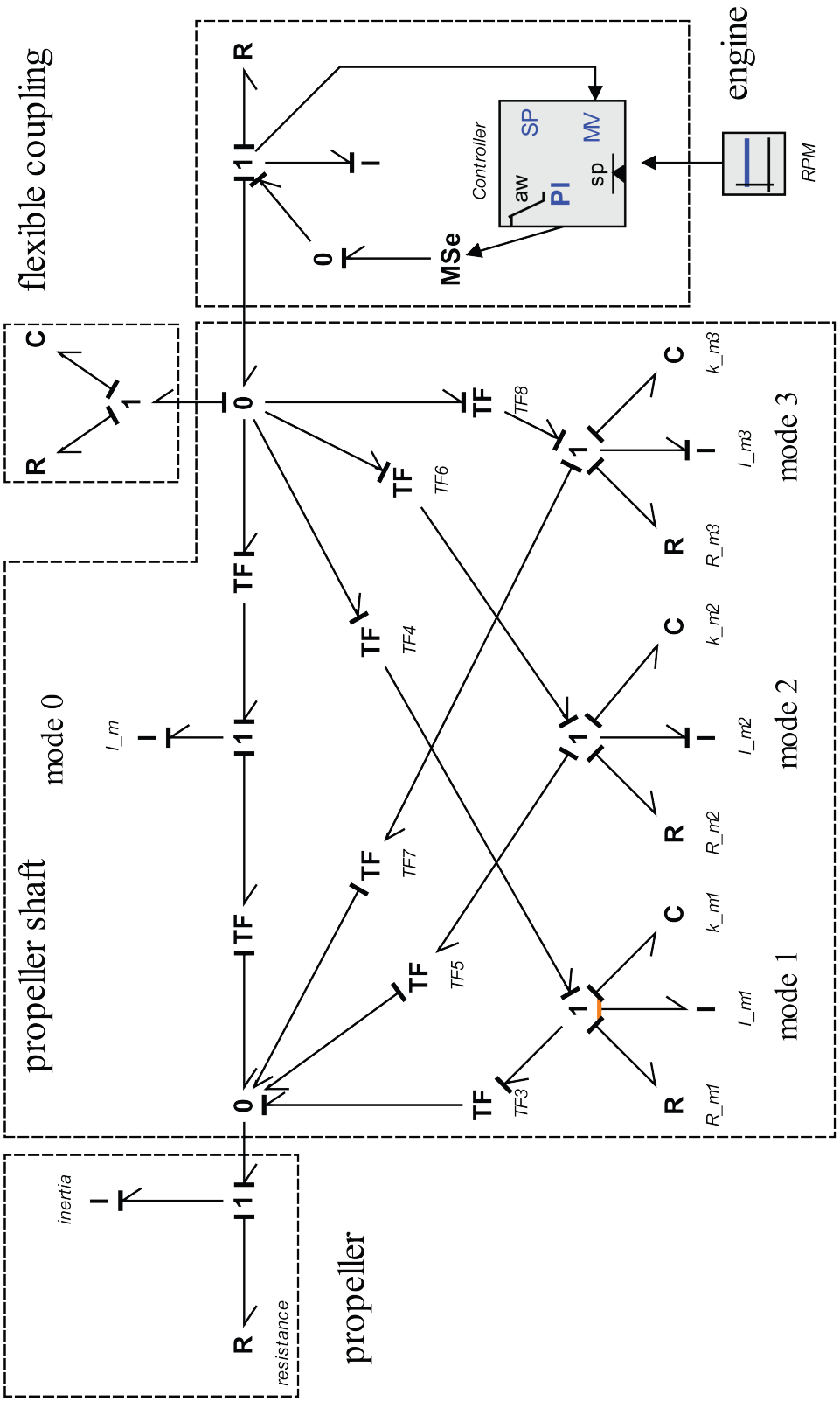

Figure 5.2: Original drive train model which the model shown in figure 5.1 based on.

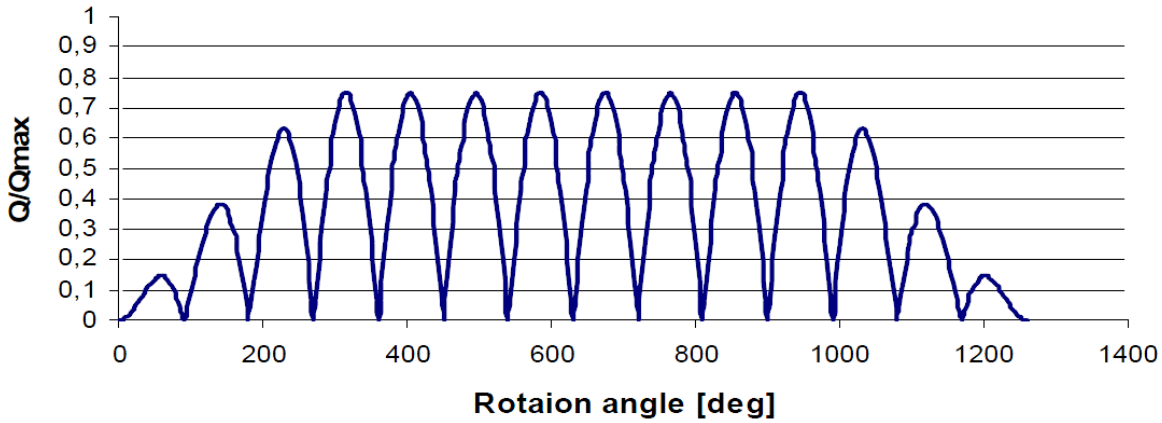

Figure 5.3: Shape of the propeller ice torque excitation for torque case 1 (DNV, 2013b). $C_q = 0.75$ $a_i = 90$

5.2 Simulation results 1

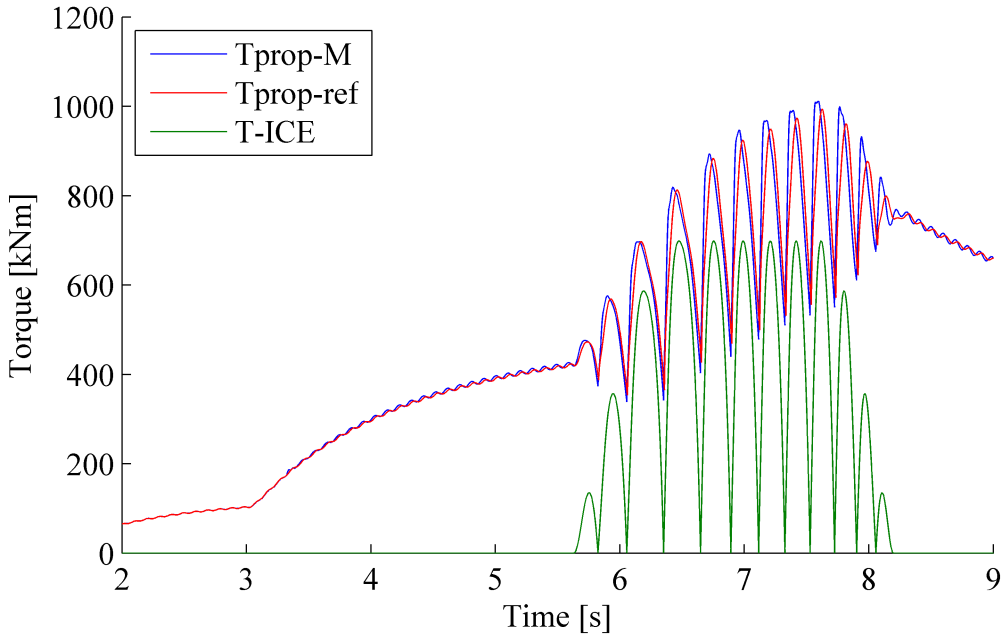

Figure 5.4: Figure showing the torque acting on the propeller using coupling-ref, $T_{Prop,ref}$ and coupling-M, $T_{prop,M}$, as the propeller is subjected to ice loads, T-ICE

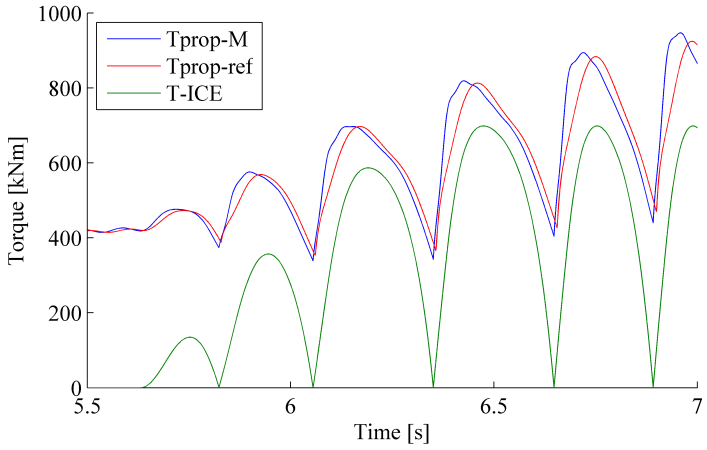

Figure 5.5: Figure showing the torque acting on the propeller during the first four ice impacts for coupling-ref, $T_{Prop,ref}$ and coupling-M, $T_{prop,M}$, as the propeller is subjected to ice loads, T-ICE.

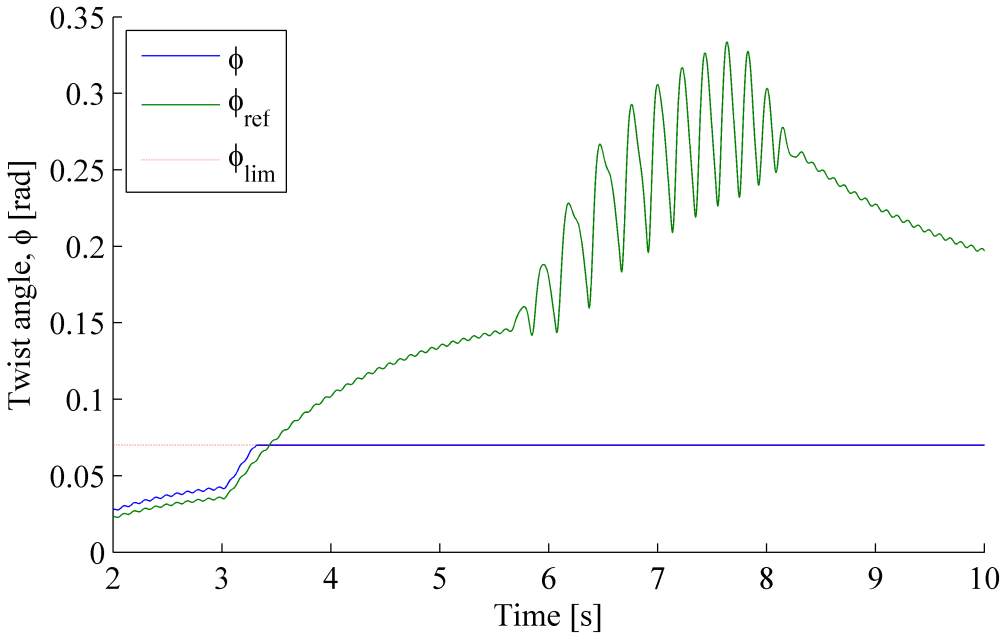

Figure 5.6: Figure showing coupling deflection of coupling-M, ϕ, and coupling-ref, ϕ_{ref}, as the propeller is subjected to ice loads. ϕ_{lim} is the twist angle at which the twist limiter is engaged.

5.3 Discussion 1

Figure 5.4 and 5.6 shows the torques acting on the propeller of the drive train model using the coupling developed in this master thesis, designated coupling-M, and the drive train model using the coupling used in (Polic et al., 2013), designated coupling-ref.

From figure 5.4 and 5.6 it can be seen that coupling-ref is under-dimensioned . Figure 5.6 shows how the maximum coupling twist, φ_{Lim}, is reached before the engine reaches full power. The consequence is that the spring hits the twist limiter , and the coupling stiffness is the same as the bumper stiffness, as explained in section 3.4

The maximum torque is constantly increasing. The reason for this is that the engine PI-controller observes that the propeller rotational velocity decreases and increases the engine torque.

By comparing the torque acting on the propeller using coupling-M, T_{Prop},with the propeller torque using coupling-ref, T_{Prop}, shown in figure 5.5. It can be seen that T_{Prop} is higher than $T_{Prop,ref}$. The reason for this is that coupling-M effectively stops

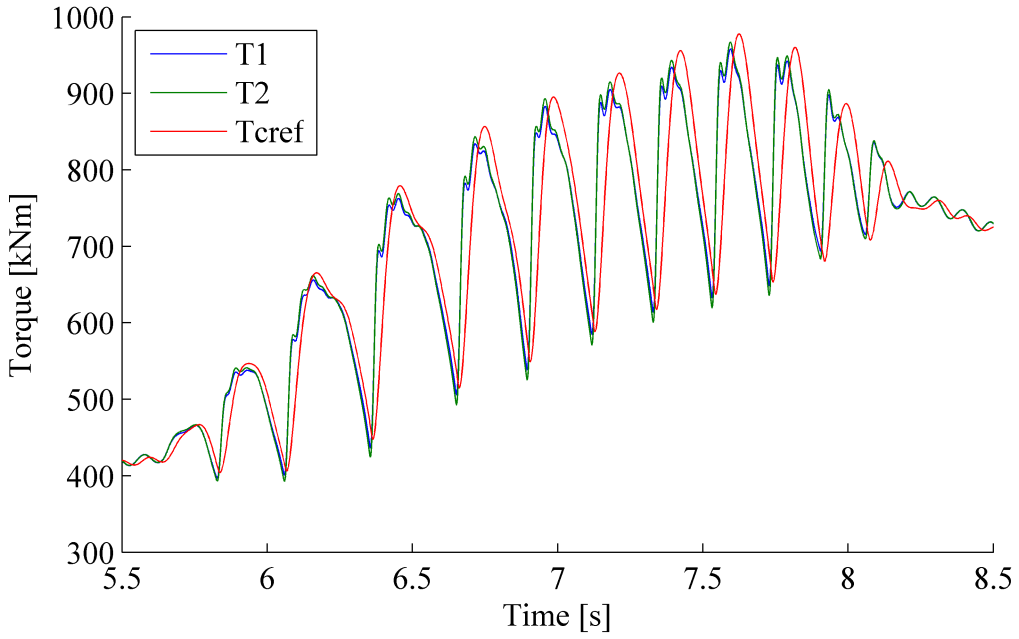

Figure 5.7: Figure showing the torque acting on the flexible coupling using coupling-ref, $T_{c,ref}$ and coupling-M, as the propeller is subjected to ice loads, T-ICE. T_1 is the torque acting on the engine side of coupling-M, while T_2 is the tourqe acting on the propeller side of the coupling

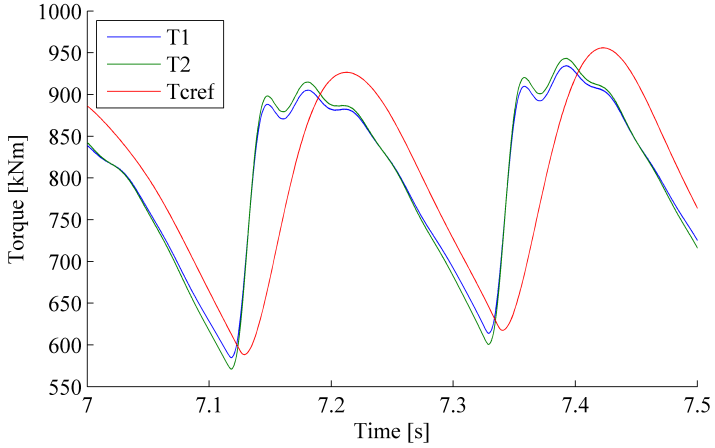

Figure 5.8: Figure showing the torque acting on the flexible coupling using coupling-ref, $T_{c,ref}$ and coupling-M, T_1 (engine side) and T_2 (propeller side) , as the propeller is subjected to ice loads, T-ICE. The figure shows the 6th and 7th ice impacts

deflecting after hitting the twist limiter. This causes the propeller velocity to change

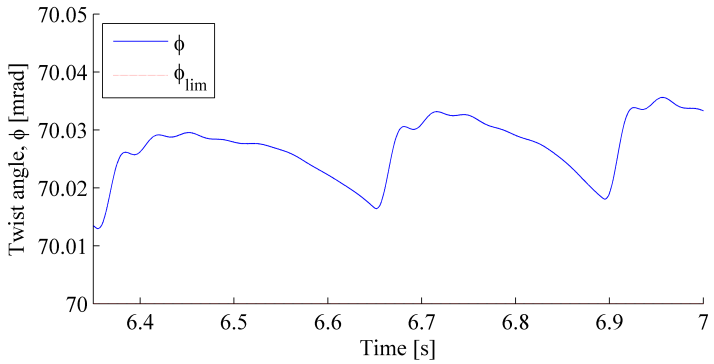

Figure 5.9: Figure showing coupling deflection of coupling-M, ϕ, as the propeller is subjected to ice loads.ϕ_{lim} is the twist angle at which the twist limiter is engaged. The figure shows the time interval of the first two ice impacts.

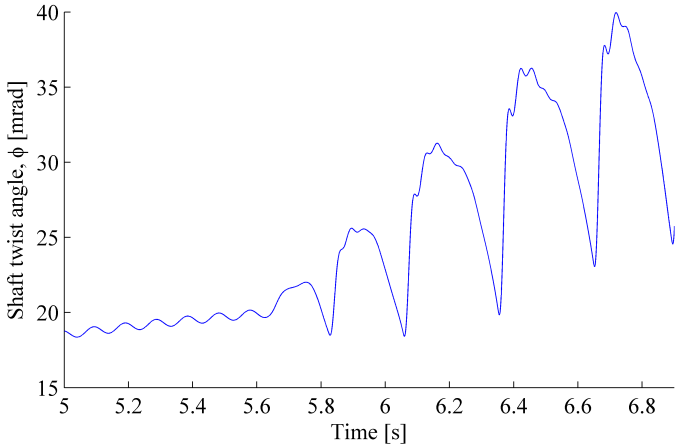

Figure 5.10: Figure showing shaft deflection, ϕ_{Shaft}, as the propeller is subjected to ice loads. The figure shows the time interval of the first five ice impacts.

faster, giving rise to higher torques.

The higher stiffness causes the incline of torque acting on coupling-M to be higher than the incline of the torque acting on coupling-ref. The torque does however not get as high as the torque acting on coupling-ref, as shown in figure 5.7 and 5.8. The reason for this is that as the lack of damping in coupling-M causes the propeller shaft to vibrate, as seen in figure 5.10 showing the shaft deflection and figure 5.9 showing the coupling deflection.

5.4 Simulation results 2

To see how the coupling performs while the twist limiter is not engaged, the number of spring/oil chamber cells was increased from 12 to 36. Figures 5.11 to5.15 shows the torque acting on the propeller and flexible coupling in addition to the coupling and shaft deflection. Figure 5.16 to 5.18 shows the pressure drop between the oil chambers, the volume flow through the slit and the chamber volume of the coupling.

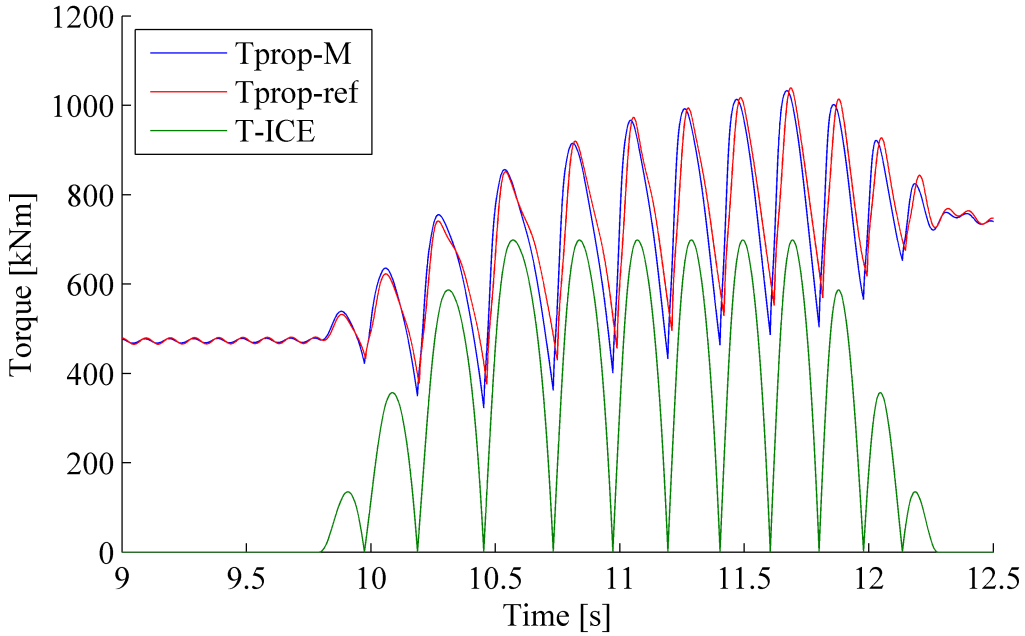

Figure 5.11: Figure showing the torque acting on the propeller using coupling-ref, $T_{Prop,ref}$ and coupling-M, $T_{prop,M}$, as the propeller is subjected to ice loads, T-ICE.

5.5 Discussion 2

By increasing the number of spring/oil chamber cells in coupling-M, from 12 - 36, the coupling stiffness is increased by a factor of 3. The coupling-ref stiffness is also increased by the same amount. This way, both the couplings have the same static stiffness. This is a way of investigating what happens when a coupling with more appropriate size is used in the drive train model without changing the drive train model.

Figure 5.11 shows the new torque acting on the propeller when including coupling-M and coupling-ref in the drive train model. Figure 5.12 shows that coupling-M does not reach the limiting twist angle. This means that it is the springs and the oil that

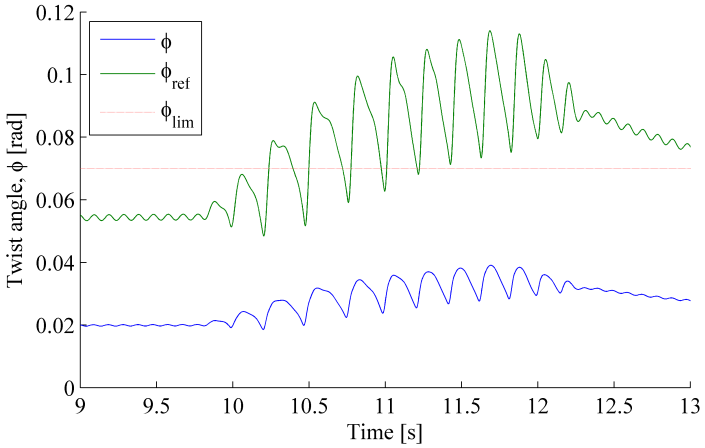

Figure 5.12: Figure showing coupling deflection of coupling-M, ϕ, and coupling-ref, ϕ_{ref}, as the propeller is subjected to ice loads. ϕ_{lim} is the twist angle at which the twist limiter is engaged.

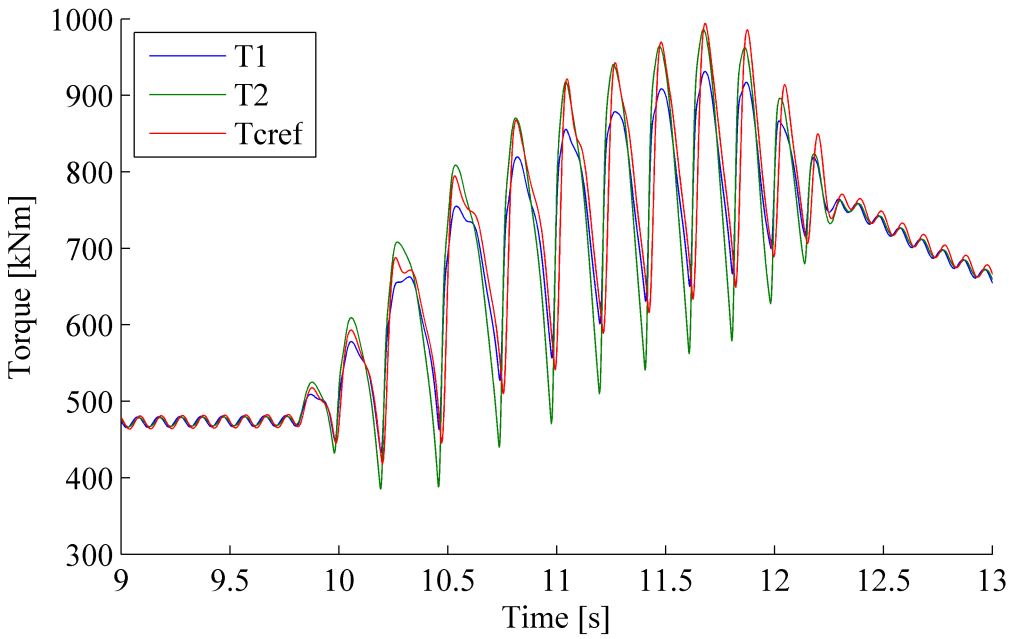

Figure 5.13: Figure showing the torque acting on the flexible coupling using coupling-ref, $T_{c,ref}$ and coupling-M. T_1 is the torque acting on the engine side of coupling-M, while T_2 is the tourqe acting on the propeller side of the coupling

causes the stiffness and not the twist limiter. The propeller torque curve is steeper for coupling-M than for coupling-ref. This is due to the effect of the oil compressibility

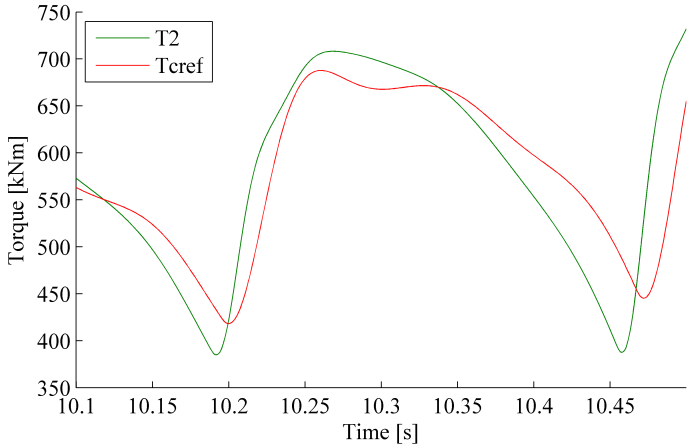

Figure 5.14: Figure showing the torque acting on the flexible coupling during the third ice impact, using coupling-ref, $T_{c,ref}$ and coupling-M, T_2

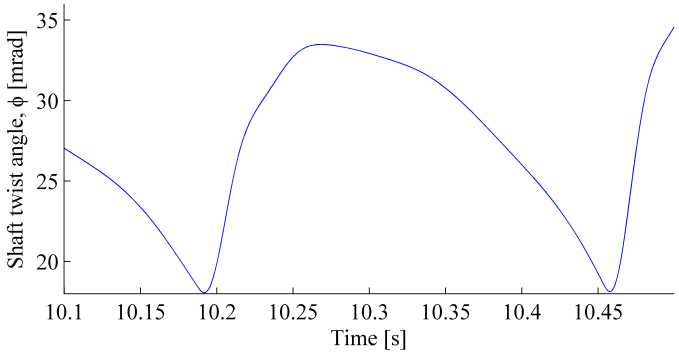

Figure 5.15: Figure showing shaft deflection, ϕ_{Shaft}, as the propeller is subjected to ice loads. The figure is zoomed up to show the time interval of the third ice impact.

increasing the stiffness of coupling-M. This is also apparent from the lower levels of couplin-M twist angle compared to coupling-ref twist angle shown in figure 5.12.

The torque acting on the engine side and propeller side of coupling-M and coupling-ref, presented in figure 5.13, shows how coupling-M isolates the peak torques from the ice-propeller interaction loads from the engine. In addition to isolating some of the engine torque pulses from the propeller side of the coupling. This is not achieved by coupling-ref.

In figure 5.14 the torque acting on the coupling coupling during third ice-propeller impact is shown. By comparing the gradients of the propeller side torque of coupling-M and coupling-ref, it can be seen that coupling-M is more stiff than coupling-ref

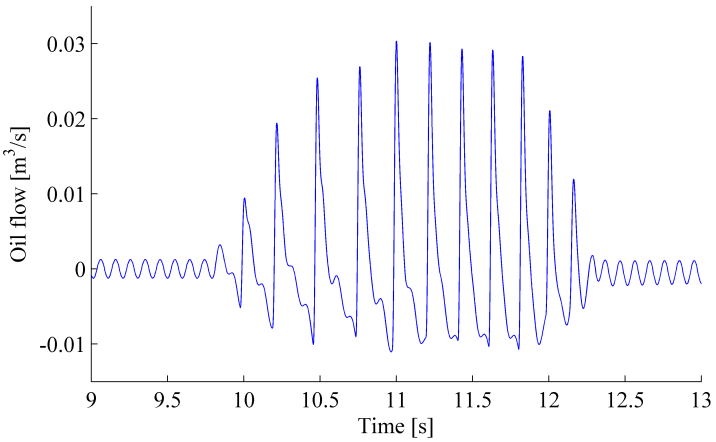

Figure 5.16: Oil flow between chamber A and chamber B of the flexible coupling during the ice impacts

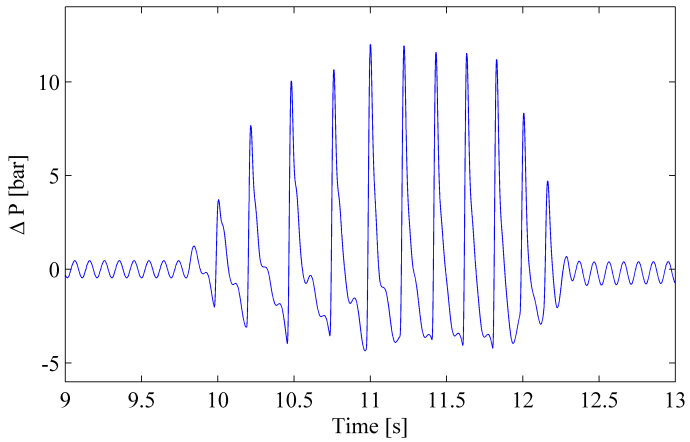

Figure 5.17: Pressure difference between chamber A and chamber B of the flexible coupling during the ice impacts

while the ice impact load increase and decrease, while coupling-M is less stiff than coupling-ref while the impact load is at its maximum. The reason for this is found by inspecting figure 5.16 and 5.17. The pressure difference between the oil chambers decreases at ones the maximum ice load is reached. The reason for this, is that the oil pressure in the oil chambers depends on the amount of oil that is compressed. The high compliance of the oil means that small change of oil causes a large change in pressure. This means that only a small amount of oil has to escape the oil chamber before the pressure change is significant. As the maximum ice impact load is reached, and the outer member of the coupling stops moving relative to the inner member, the pressure is at it highest causing a high volume flow between the chambers. Since the

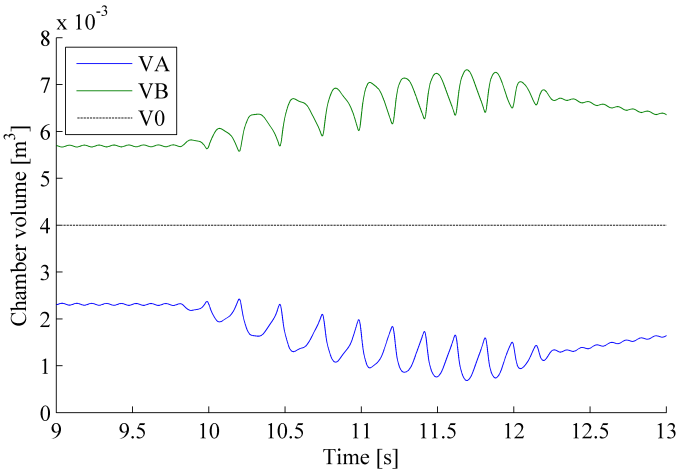

Figure 5.18: Volume of the oil chamber as the flecible coupling deflects due to the ice impact loads. VA is the volume of chamber A, VB is the volume of chamber B and V0 is the initial volume of the chambers.

geometric volume of the oil chamber has stopped changing at this point as shown in figure 5.18, will volume flow out of the chamber cause pressure to drop quickly. This means that the pressure force acting on the spring is lower and the coupling stiffness is closer to the static stiffness. As the volume starts changing again due to the decreasing ice impact load, the pressure difference increases, resulting in higher stiffness.

By comparing the shaft twist in figure 5.15 to the shaft twist in section 5.10, it can be seen that the vibrations are avoided by increasing the stiffness of the coupling and avoiding the twist limiter being engaged.

Chapter 6

Conclusion and Recommendations for Further Work

6.1 Conclusion

A model of a Geislinger type flexible coupling was developed using the bond graph approach. The model includes radially aligned springs modelled using finite mode superposition. Unlike the actual Geislinger flexible coupling which have springs with tapered cross section, are the springs in the model included using constant cross section. The effect of the oil compressibility is also included. In addition, is the pressure drop as the oil flows between the chambers included in the flexible coupling bond graph model.

Some of the parameters used in the model are given explicitly by the flexible coupling manufacturer. However, most of the geometric parameters are not given explicitly, and were found by approximation within the limits given by the flexible coupling manufacturer.

The coupling manufacturer provides stiffness and damping coefficient values at a range of excitation frequencies. Simulations show that the stiffness at zero frequencies is obtainable by changing the radius of the inner member, the radius of the outer member and the height of the spring profile.

Using the spring profile height giving correct static stiffness, the first natural frequency of the spring was found to be outside of the operating range of the flexible coupling. The springs flexible modes was therefore omitted from the model.

Simulations showed that the coupling stiffness increases with frequency within the frequency range investigated. The reason for this is that the amount of oil that is compressed increases at higher frequency due to higher pressure drop as the oil travels from one chamber to another. The gradient of the stiffness decreases at higher fre-

quencies. The reason for this is that the increased stiffness at higher frequency causes the oil chamber volume to change less.

In addition, did the simulations show that the damping factor increases with frequency, while the gradient decreases. The reason for this is that the maximum potential energy of the coupling during one loading cycle decreases at higher frequencies. This is due to the increasing stiffness and that the energy dissipated during one loading cycle decreases after reaching a maximum value. The reason for the dissipated energy to decrease. is that the increased stiffness causes the amplitude of the coupling deflection to decrease at higher frequencies.

The damping factor and dynamic stiffness were found to be to high, compared to the data given by the manufacturer. The parameter that has the highest effect on the frequency response is the coefficient of discharge. This is since this controls the amount of oil that escapes the oil chamber at a given pressure. Simulations did show that by increasing the coefficient of discharge produced similar damping and stiffness coefficients as the values given by the manufacturer. This does not mean that the parameters chosen are correct, as a number of parameter combinations would give the same results.

The bond graph model of the flexible coupling was implemented in a bond graph model of a marine propulsion drive train, subjected to ice impact loads. Simulations did show that the coupling stiffness was to low for excitation torque of the engine, so that the twist limiter was engaged before the ice impacts occurred. This caused the coupling to adopt the stiffness of the twist limiter and the damping characteristics of the flexible coupling was lost, causing vibrations in the shaft.

The simulations were also performed by using a flexible coupling model with an increased number of spring/oil chamber cells. During these simulations, the twist limiter was not engaged. The simulation results did show that the flexible coupling model developed in this master thesis had a higher stiffness than the flexible coupling model used for comparison. The stiffness was higher while the ice load gradient was large, and while the load changed direction the stiffness became lower than the reference model. The reason for this is that the oil compressibility causes the pressure acting on the springs to decrease at once the oil chamber volume stops changing.

6.2 Recommendations for Further Work

The effect air trapped in the oil has on the compressibility of the oil is not included in this model . This should be further investigated since this will cause the total compressibility of the oil to change significantly under low pressures, which occur during

impulse loads acting on the flexible coupling. In addition is the radially aligned springs included without changing cross sectional area. The effect of the changing cross sectional area is highest at large deflections, and should therefore be included to get the correct response during impulse loads.

The vibratory excitation torque from the engine is modelled as a simple harmonic function. Since the coupling characteristics were shown to change based on the nature of the excitations is it recommended that a more realistic excitation torque is included to investigate the response during impulsive loads.

The pressure-flow relation describing the volume flow between the chambers used in the model was assumed to follow the orifice equation. As the pressure-flow relation is one of the major effects that controls the coupling characteristics is it recommended that CFD simulations are performed to verify the pressure flow relation.

Bibliography

Borutzky, W. (2010). *Bond graph methodology: development and analysis of multidisciplinary dynamic system models*. Springer, London.

Castrol (2012). Mhp range engine lubrication oil data sheet.

DNV (2008). Rules for ships / high speed, light craft and naval surface craft - pt.4 ch.4 sec.5 - a203.

DNV (2013a). Ships for navigation in ice.

DNV (2013b). Ships for navigation in ice - pt5 ch.1 sec.3.

Çengel, Y. A., Cimbala, J. M., and Kanoğlu, M. (2010). *Fluid mechanics: fundamentals and applications*. McGraw-Hill, Boston. 1 DVD-ROM (12 cm) i lomme 2nd ed. in SI units.

Erikstad, S. and Ehlers, S. (2012). Decision support framework for exploiting northern sea route transport opportunities. *Ship Technology Research*, 59(2):34–42. cited By (since 1996)1.

Geislinger (2013). Geislinger coupling catalog version 17.6.

Hodges, P. K. B. (1996). *Hydraulic fluids*. Arnold, London. "Revised edition of the original Norwegian language publication issued in 1994"–Pref.

Johannessen, J. (2002). *Tekniske tabeller*. Cappelen, [Oslo]. Fra 4. oppl. 2006 med både 10- og 13-sifret ISBN Utg. nr 2.

Karnopp, D., Margolis, D. L., and Rosenberg, R. C. (2012a). *System dynamics: modeling, simulation, and control of mechatronic systems*. Wiley, Hoboken, N.J. Tilgang via Internett 5th ed.

Karnopp, D. C., Margolis, D. L., and Rosenberg, R. C. (2012b). *System Dynamics: Modeling, Simulation, and Control of Mechatronic Systems: Fifth Edition*. Cited By (since 1996):2 Export Date: 28 November 2013 Source: Scopus.

McCloy, D. and Martin, H. R. (1980). Control of fluid power: Analysis and design. 2nd (revised) ed. Cited By (since 1996):31.

Pedersen, E. and Engja, H. (2008). *Mathematical modelling and simulation of physical systems: lecture notes in course TMR4275 Modelling, simulation and analysis of dynamic systems*, volume UK-2008-[10]5. Marinteknisk senter., Trondheim.

Pedersen, E. Valland, H. (2013). Lecture notes in mechanical vibrations courses tmr4222 and tmr4223.

Polic, D., Æsøy, V., Ehlers, S., and Pedersen, E. (2013). *Propulsion machinery operating in ice: a modelling and simulation approach*, pages S. 191–197. ECMS, [San Diego, CA].

Veitch, B. (1995). *Predictions of ice contact forces on a marine screw propeller during the propeller-ice cutting process*, volume no. 118. Finnish Academy of Technical Sciences., Helsinki.

Wang, J. (2007). Thesis.

Wang, J., Akinturk, A., Jones, S. J., Bose, N., Kim, M. C., and Chun, H. H. (2007). Ice loads acting on a model podded propeller blade (omae2005-67416). *Journal of Offshore Mechanics and Arctic Engineering*, 129(3):236–244. Cited By (since 1996):3 Export Date: 27 November 2013 Source: Scopus.

Appendix A

Coupling parameters for the reference model

A.1 Coupling parameters given by the manufacturer

The parameters given by the manufacturer in the coupling catalogue Geislinger (2013).

Parameter	Value	Unit	Symbol
Nominal torque	218	[kN m]	T_{KN}
Static torsional stiffness	4.7	[MN m rad^{-1}]	C_{Tstat}
Characteristic coupling frequency	690	[rad s^{-1}]	ω_0
Permissible damping torque	3620	[N m bar^{-1}]	$T_{d.p}$
Radial misalignment	0.9	[mm]	ΔK_r
Rotational inertia of inner member	21.70	[kg m^2]	J_1
Rotational inertia of outer member	305	[kg m^2]	J_2
External diameter	1.10	[m]	D
Coupling width	0.249	[m]	B
Width of the spring pack	0.10	[m]	w_{Spring}
Twist at nominal torque	0.045	[rad]	$\varphi_{Nominal}$

Table A.1: Coupling parameters given by the manufacturer for coupling - BC 110/10/45 UC/L (Geislinger, 2013)

A.2 Measured Coupling Dimensions

The measured dimensions are shown in figure A.1,A.3 and A.4. The measured dimensions are also listed in table A.2.

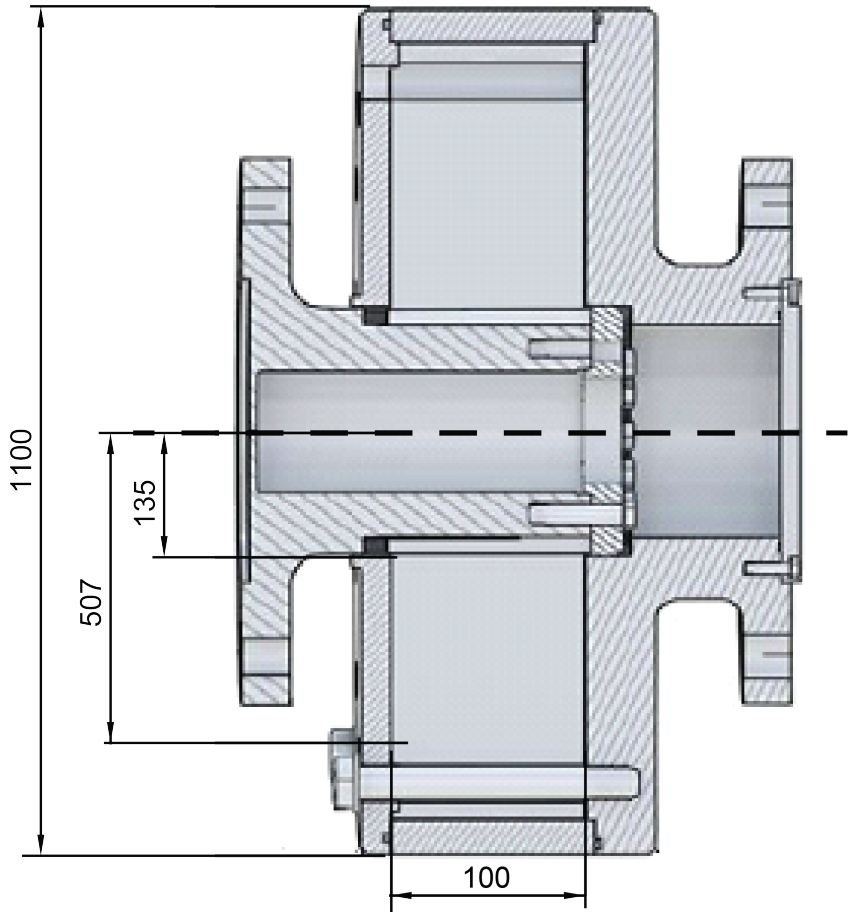

Figure A.1: Drawing of the coupling from the catlaogue (Geislinger, 2013), scaled to the measurements of the BC 110/10/45 UC/L-Coupling. Side view. Measurements in mm

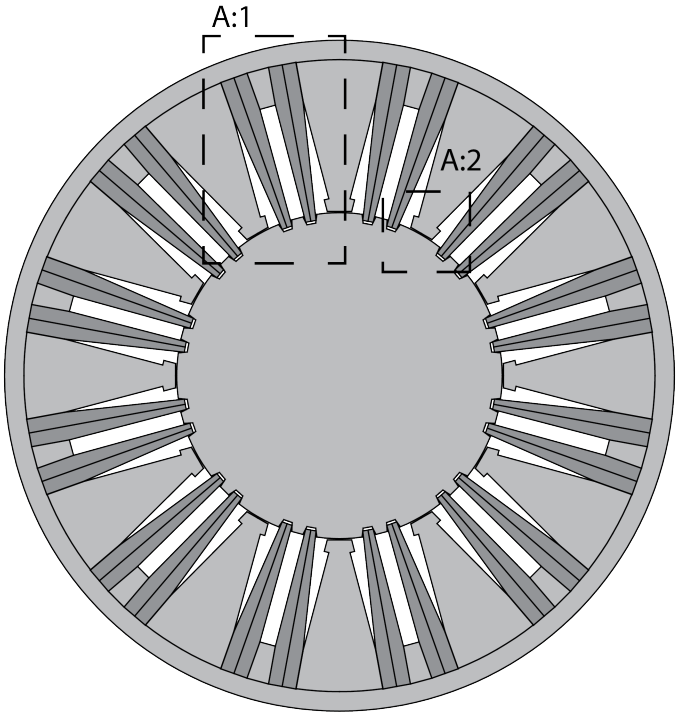

Figure A.2: Drawing of the coupling from the catlaogue (Geislinger, 2013), scaled to the measurements of the BC 110/10/45 UC/L-Coupling. Front view

Parameter	Value	Unit	Symbol
Number of cells	12	[-]	n_cell
Inner radius of chamber	0.135	[m]	r_1
Outer radius of chamber	0.507	[m]	r_2
Height of the spring at the inner end	0.046	[m]	h_1
Height of the spring at the outer end	0.017	[m]	h_2
Distance between the twist limiter and spring	0.020	[m]	D_{Lim}
Length of twist limiter	0.010	[m]	L_{Bump}
Heigth of twist limiter	0.020	[m]	h_{Bump}
Distance from center of twist limiter to r1	0.012	[m]	r_{Bump}
Maximum twist	0.070	[rad]	φ_{Lim}

Table A.2: Geometric parameters measured from upscaled drawing

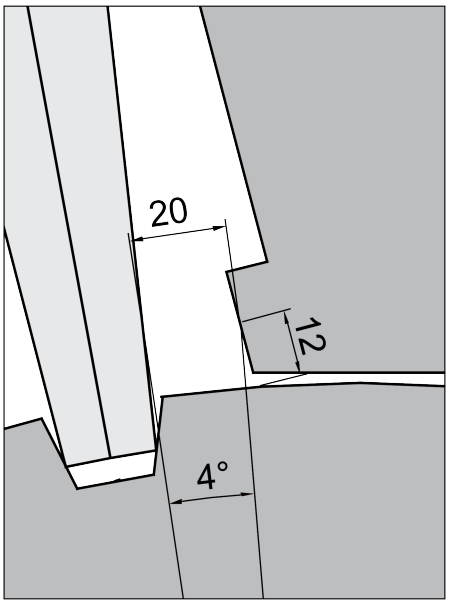

Figure A.3: Drawing of the coupling from the catlaogue (Geislinger, 2013), scaled to the measurements of the BC 110/10/45 UC/L-Coupling. View A:1. Measurements in mm

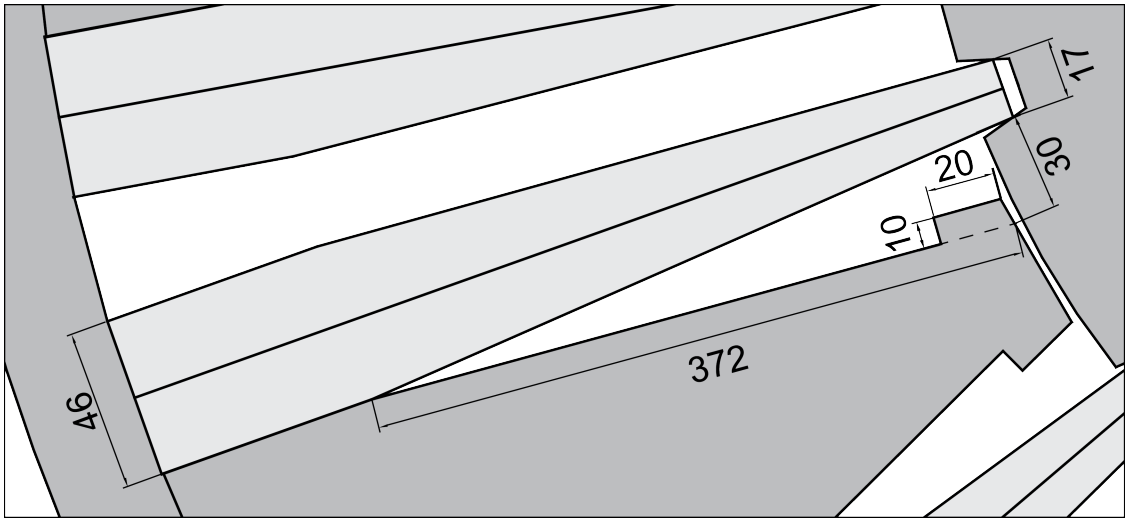

Figure A.4: Drawing of the coupling from the catlaogue (Geislinger, 2013), scaled to the measurements of the BC 110/10/45 UC/L-Coupling. View A:2. Measurements in mm

A.3 Calculated coupling parameters

The geometric parameters in table A.3 are found using equations A.1 - A.8.

Parameter	Value	Unit	Symbol
Effective length of spring	0.372	[m]	L_{Spring}
Average height of the spring	0.0315	[m]	h_{Spring}
Average area of the spring profile	0.00315	[m^2]	A_{Spring}
Average polar moment of inertia of the spring profile	2.6e-7	[m^4	$I_{Profile}$
Area of the slit	0.00009	[m^2]	A_{Slit}
Tangential projection of the inner wall area of the chambers	0.0372	[m^2]	A_T
Distance between r_1-r_2 and the coupling axis	0.321	[m]	r_P
Initial oil chamber volume	0.000538	[m^3]	V_0

Table A.3: Geometric parameters of the coupling found using equations A.1 - A.8.

Effective spring length:

$$L_{Spring} = r_2 - r_1 \tag{A.1}$$

Average height of the spring:

$$h_{Spring} = \frac{h_1 + h_2}{2} \tag{A.2}$$

Average area of the spring:

$$A_{Spring} = h_{Spring} \cdot w_{Spring} \tag{A.3}$$

Average polar moment of inertia of the spring profile:

$$I_{Spring} = \frac{w_{Spring} h_{spring}^3}{12} \tag{A.4}$$

Area of the slit:

$$A_{Slit} = \Delta K_{Slit} w_{Spring} \tag{A.5}$$

Tangential projection of the inner wall of the oil chambers:

$$A_T = (r_2 - r_1)\, w_{Spring} \tag{A.6}$$

Distance between the area center of the chamber and the coupling axis:

$$r_p = r_1 + \frac{r_2 - r_1}{2} \tag{A.7}$$

Initial oil chamber volume

$$V_0 = \left(L_{Spring} \cdot (D_{Bump} + L_{Bump})\, \frac{1}{2} - (L_{Bump} h_{Bump}) \right) w_{Spring} \tag{A.8}$$

A.4 Spring parameters

In (Johannessen, 2002), the modulus of elasticity and density of steel is given as shown in table A.4.

Parameter	Value	Unit	Symbol
Youngs modulus of the spring material	200	[GPa]	E
Density of spring material	7850	[kg m^{-3}]	ρ
Modal damping ratio	0.01	[-]	ξ

Table A.4: Spring parameters

A.5 Hydraulic parameters

A.6 Bumper parameters

The axial deformation related to the force acting on the twist limiter is (**?**):

$$w_B = F\frac{L_B}{A_B E} \tag{A.9}$$

w_B	Deformation of twist limiter
F	External force acting on twist limiter
L_T	Length of the twist limiter seen as flexible
A_T	Area of the twist limiter facing the spring
E	Modulus of elasticity of the twist limiter material

Where the force acting on the twist limiter found from using the torque acting on one spring/chamber cell T/n and the distance between the center of the twist limiter to the center of the coupling axis r_b:

$$F = \frac{T}{r_B n} \tag{A.10}$$

Which give the maximum stiffness of the twist limiter as:

$$K_{Max} = n r_B \frac{A_B E}{L_B} \tag{A.11}$$

Using the dimensions in table A.3 and A.3 the stiffness is: 7.056e10 [N m rad^{-1}]
The angle between where the radial spring hits the twist limiter and the twist limiter is measured in the same manner as described in section 4 and found to be 4°or 0.07 rad as shown in section A.2, figure A.3.